Field Ionization and Field Emission
with Intense, Single-cycle THz Pulses
Need to replace with my own title

by

© Yunxiao Wang

A thesis submitted to the

School of Graduate Studies

in partial fulfilment of the

requirements for the degree of

Anqing, Anhui, China

B.S. in Physics University of Science and Technology of China May 2009

Memorial University of Newfoundland

Doctor of Philosophy

St. John's   Newfoundland

Department of Physics August, 2016

Abstract

Nuclear-polarized ^{3}He targets have been widely used in electron-scattering experiments in Thomas Jefferson National Accelerator Facility (JLAB) since mid 1990s. It is of great importance to produce large amounts of ^{3}He gas with high polarization.

The latest experiments run in JLAB prior to the 12GeV upgrade have been using cells polarized with Spin-Exchange Optical Pumping (SEOP). These cells were made of the GE180 glass and use a two-chambered design. The top chamber, known as the pumping chamber, is where ^{3}He is polarized through SEOP. The bottom chamber, known as the target chamber, is where electron scattering occurs. Great effort has been made in our lab to develop this generation of cells. Alkali-hybrid SEOP together with narrowband laser diode arrays have increased the ^{3}He polarization from 37% to 65%. Among other things, we also carefully studied an additional spin relaxation mechanism that limits the maximum achievable ^{3}He polarization.

The 12GeV upgrade makes the future experiments much more demanding in terms of target cell performance. One challenge it brings is the high relaxation due to electron beam. We have designed and tested a new style cell that uses convection instead of diffusion to increase the rate at which the polarization in the target chamber is being replenished by gas from pumping chamber. We have obtained over 50% polarization with controllable convection speed so far.

An additional problem that comes with higher beam current is that the glass end windows of traditional design are not likely to survive the experiments. Our group started exploring the option of using metal end windows from a decade ago. The first problem to solve is to find out the correct material and the proper technique

to incorporate metal without introducing significant spin relaxation and still being able to hold high pressure gas (12 atm) inside. This is a brand new technique that may have a profound impact of future cell designs once fully developed. Although no metal end windows have been tested so far, multiple glass cells with different kinds metal tubes (much larger in area compared to the end windows that will be used in JLAB experiments) attached were examined and were enough to convince us the extra spin relaxation is not likely to cause significant problems. The metals tubes were connected to Pyrex glass with knife-edge (housekeeper) seals and stayed intact through high pressure tests. After exploring options such as pure copper, gold coated copper, titanium, stainless steel, gold coated titanium, we have established that electroplating gold on copper substrate yields the best result so far. Further tests are planned before attaching metal end windows to GE180 glass and using them in electron-scattering experiments.

Acknowledgements

Put your acknowledgements here...

"Intellectual and practical assistance, advice, encouragement and sources of monetary support should be acknowledged. It is appropriate to acknowledge the prior publication of any material included in the thesis either in this section or in the introductory chapter of the thesis."

— MUN School of Graduate Studies

Contents

List of Tables

List of Figures

Chapter 1

Spin-Exchange Optical Pumping

1.1 Overview

Spin-polarized noble gases have been widely used for various purposes. In JLAB, polarized ^{3}He is used as target for electron-scattering experiments. This is because a ^{3}He nucleus has a pair of protons with paired spins and a single neutron that contributes the most of the nuclear spin. In MRI, polarized ^{3}He has seen uses such as detecting structural damage in the lungs.

There are generally two ways of polarizing ^{3}He: Metastability-Exchange Optical Pumping (MEOP) and Spin-Exchange Optical Pumping (SEOP). Our group focuses on SEOP as MEOP polarizes gas at relatively low pressure ($\sim$1 torr), thus further compression is required to produce target cells of several atms that meet the need of JLab experiments.

In SEOP, alkali metal is polarized by circularly polarized laser tuned to the D1 transition of the particular alkali species used. ^{3}He obtains polarization from alkali

metal through spin exchange process. With the combination of hybrid alkali mixtures (typically Rb and K) and spectrally narrowed lasers, more than 70% polarizations have been produced.

1.2   Optical pumping

1.2.1   Rb for SEOP

In optical pumping, Rb is often the alkali metal chosen to be optically pumped by circularly polarized laser light. The angular momentum of a polarized photon is transfered to the valence electron of Rb atom. In the case of hybrid mixture of Rb/K, Rb is still the alkali metal that is directly pumped by laser light while K serves as an efficient medium to transfer the polarization from Rb to ^{3}He. Because the spin destruction rates are much lower for lighter alkali metals, K-^{3}He spin-exchange process is a lot more efficient than that of Rb-^{3}He. However, it is still much easier to optically pump Rb and transfer the polarization to ^{3}He through K, mainly for Rb's low melting point, the relative ease of acquiring laser at the Rb D1 line wavelength and the wide separation between D1 (794.7nm) and D2 line (780nm).

The Rb melting point is at 39.5°C, so it's easy to achieve enough Rb vapor without having to drive the oven temperature too high. In our lab, depending on if the cell contains pure Rb or Rb/K mixture, the oven temperature can be between 85°C to as high as 255°C. Perhaps the most used oven temperature for hybrid is 235°C which has empirically been a good temperature to produce Rb/K mixture vapor, while 85°C is enough for pure Rb.

1.2.2 Vapor Pressure Curves

When the alkali metal is heated to above its melting point, a small amount of alkali metal atoms evaporate. The equilibrium vapor pressure is temperature dependent:

$$P = 10^{5.006+\alpha+\beta/T} Pa \tag{1.1}$$

where α and β are listed in Table 1.2.2.

	Patassium	Rubidim
α	4.402	4.312
β	-4453	-4040

Thus the number density is

$$[A] = \frac{10^{5.006+\alpha+\beta/T}}{k_B T} \tag{1.2}$$

The number density curves of pure Rb and K vapor are shown in Fig. 1.1.

1.2.3 Energy Levels of Alkali Metal in External Magnetic Field

The Hamiltonian for ground state (L=0) alkali metal atoms in external magnetic field is:

$$\mathbf{H} = A\mathbf{I} \cdot \mathbf{S} + g_e\mu_B S_z B_z + g_N\mu_N I_z B_z \tag{1.3}$$

The first term $A\mathbf{I} \cdot \mathbf{S}$ describes the coupling of the nuclear spin $\mathbf{I}$ with the electron spin $\mathbf{S}$ and is key to spin exchange, where A is the isotropic magnetic-dipole coupling
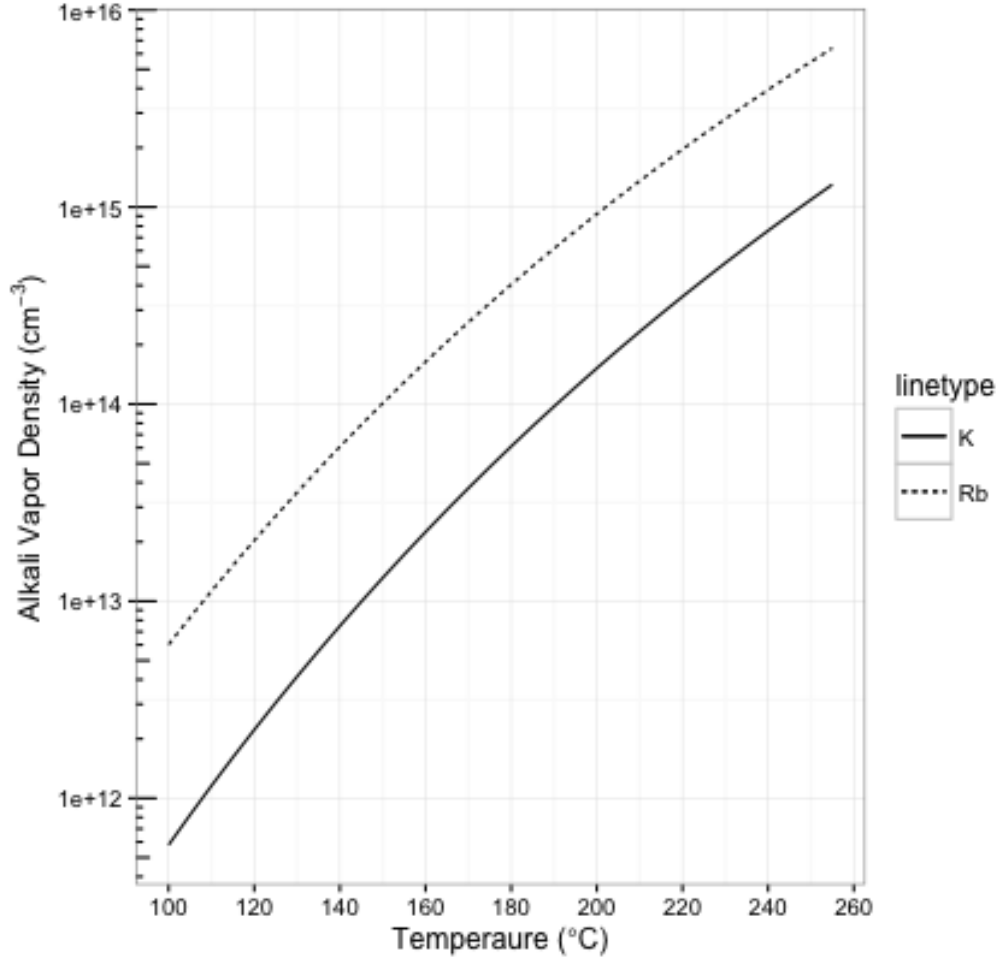
Figure 1.1: Rb And K Number Density Curves

coefficient. The resulting energy levels from the first term are referred to as hyperfine structure. The second and third terms describe the Zeeman splitting due to the presence of a weak external magnetic field. $\mu_B = 9.274 \times 10^{-24} J/T$ and $\mu_N = 5.051 \times 10^{-27} J/T$ are the Bohr and nuclear magnetons. $g_e \approx 2$ and $g_N \approx 5.59$ are the electronic and nuclear Lande g-factors.

The linear relationship between energy levels and magnetic field only holds for weak magnetic fields which applies to our lab where $\sim$13 Gauss is used most of the

time. When the Zeeman splitting grows comparable to the hyperfine energy difference one would have to take into account the quantum mixing of the states, the result is described by Breit-Rabi Formula. With ~13 Gauss, the hyperfine term dominates the total Hamiltonian. The energy levels of ^{87}Rb are shown in Fig. 1.2.

1.2.4 Optical Pumping Process Overview

For simplicity, the following discussion will ignore the nuclear spins for now. The inclusion of nuclear spins will increase the number of energy states but the optical pumping mechanism remains the same. In our typical setup, circularly polarized laser light is tuned to the D1 line of Rb and excites valence electrons of Rb from $5S_{1/2}$ state to $5P_{1/2}$ state as shown in Fig. 1.3 ($2S_{1/2}$ and $2P_{1/2}$ states are used in the simple model described by the figure below).

Left-circularly polarized light is assumed in the figure, but either circular polarization works the same. Conservation of angular momentum requires $\Delta m = +1$ as the figure shows. Through collisions with other Rb atoms, excited electrons will mix and evenly distribute on the two $2P_{1/2}$ states. Electrons then decay to the two ground states with equal probabilities. The selection rule for the decay process is $\Delta m = 0$ or ± 1. Even though both ground states receive electrons from the decay, only the m = -1/2 state absorbs the circular polarized photons and is being depleted, so atoms are in effect pumped to the m = +1/2 state. When we consider Rb with nuclear spins, both $5S_{1/2}$ and $5P_{1/2}$ states are split into more energy levels, but the net effect is still that the ground state with highest m accumulate atoms over time.

When the excited electrons decay back to the ground state, they emit unpolarized
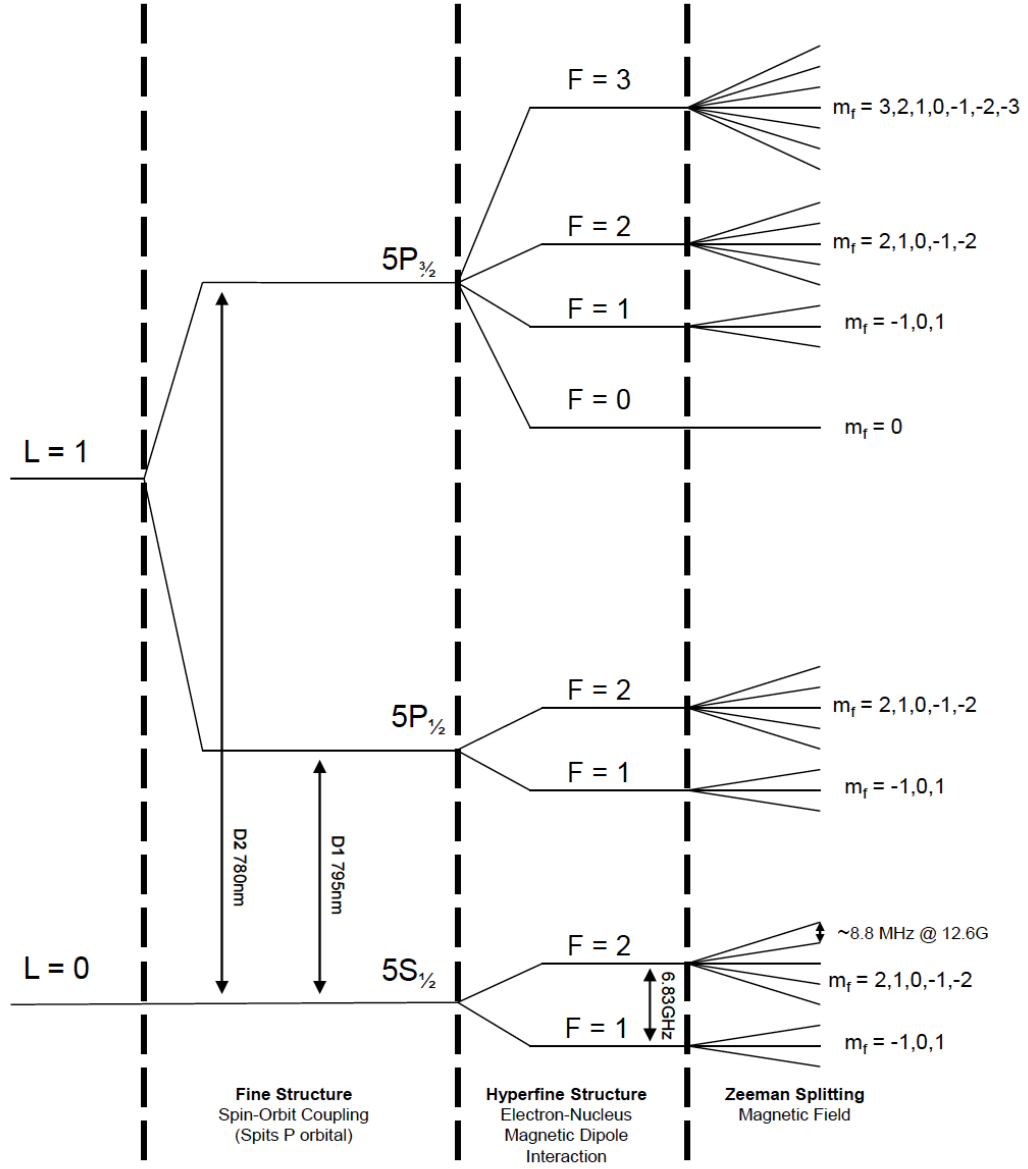
Figure 1.2: Level Diagram of ^{87}Rb. The splittings are not to scale. Adapted from Dolph's PhD thesis.

photons with angular momentum in random directions which can depolarize the gas. A small amount of N_2 gas is added into the cell (typically around 0.1 Amagats) to non-radiatively quench the excited electrons as N_2 molecules can absorb the released
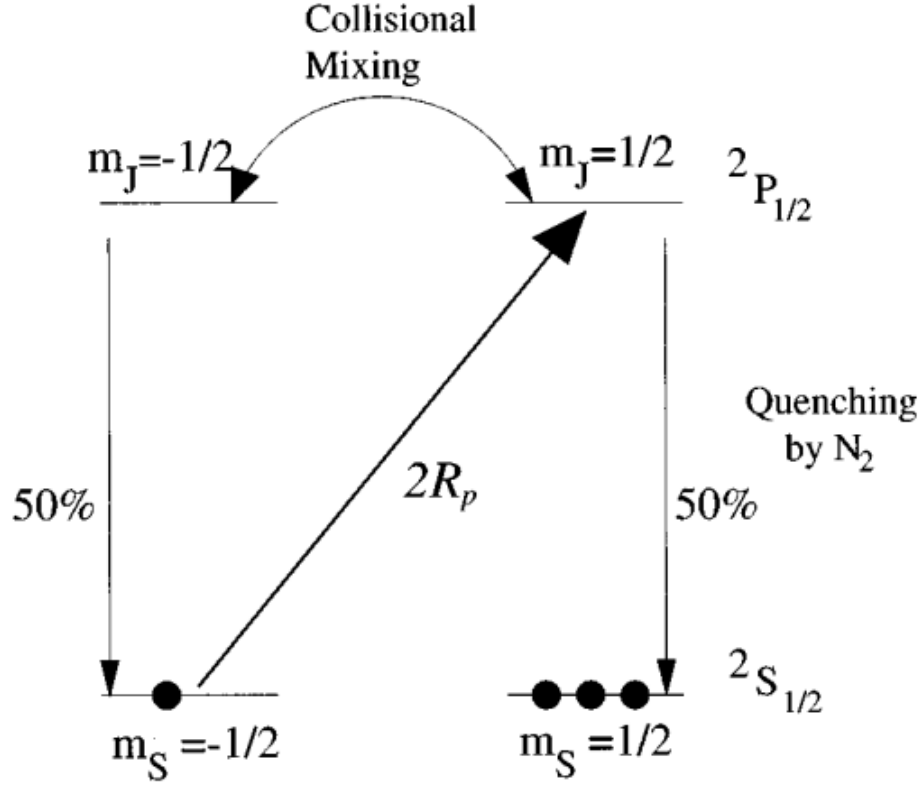
Figure 1.3: The interaction of alkali-metal atoms with left-circularly (σ^+) polarized light. (from Ref. [10])

energy of spontaneous decays into their rotational and vibrational modes of oscillation. With an appropriate amount of N_2, the photon-emitting decays can be reduced to less than 5%.

1.2.5 Optical Pumping Rate

The optical pumping rate at position $\vec{r}$ can be described by

Table 1.1: Pressure broadening of Rb D_1 lines by ^{3}He, ^{4}He and N_2. The broadening and shifting density coefficients are listed. The 4th and 6th columns are the temperature dependence for He and N_2, respectively. All coefficients are given for 353 K, values for different temperatures can be calculated with the temperature dependence.

	^{4}He	^{3}He	Temp. depen.	N_2	Temp. depen.
D_1 full width (GHz/amg)	18.0±0.2	18.7±0.3	$T^{0.05\pm0.05}$	17.8±0.3	$T^{0.3}$
D_1 line shift (GHz/amg)	4.3±0.1	5.64±0.15	$T^{1.1\pm0.1}$	-8.25±0.15	$T^{0.3}$

$$R = \int \Phi(\nu, \vec{r})\sigma(\nu)d\nu \tag{1.4}$$

where $\Phi(\nu, \vec{r})$ is the position dependent photon spectral flux density and $\sigma(\nu)$ is the photon absorption cross section. The cross section has a natural Lorentzian lineshape which is broadened by Doppler effect and pressure broadening. The pressure broadening effect dominates the lineshape as our cells normally have densities well above one amagat. The collisions of Rb with ^{3}He and N_2 cause the broadening as well as a slight shift of the D_1 line. The coefficients of pressure broadening for ^{3}He, ^{4}He and N_2 are listed in Table 1.1, and can be used to calculate the broadened line width and the shifted line center.

$\sigma(\nu)$ follows the sum rule:
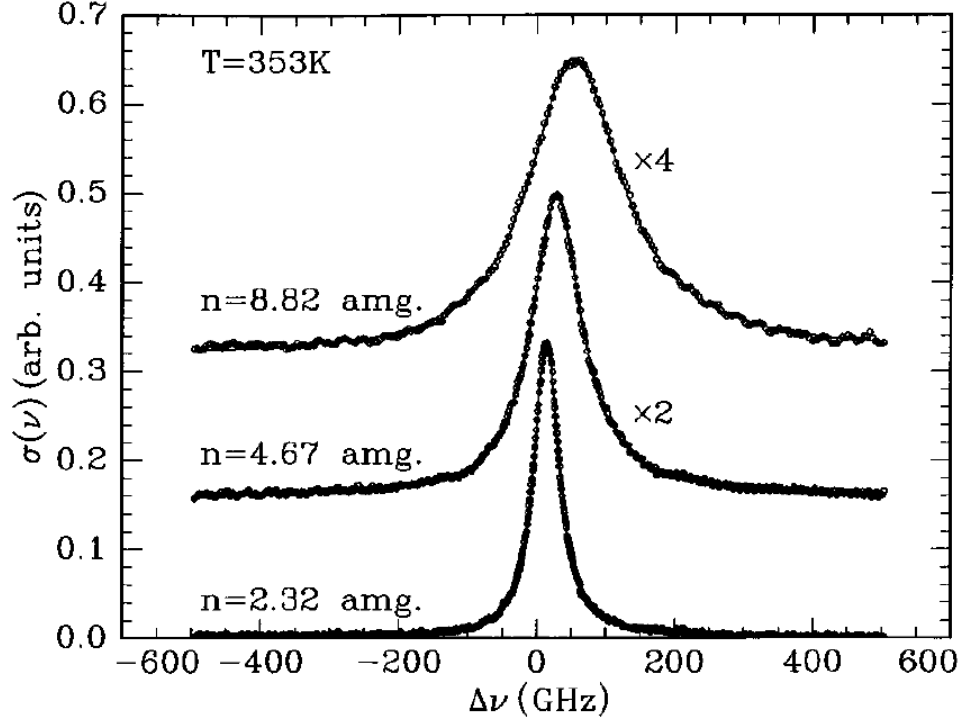
Figure 1.4: Absorption cross section for Rb D_1 line in the presence of three different densities of ^{3}He. (from Ref. [6])

$$\int \sigma(\nu)d\nu = \pi r_0 cf \tag{1.5}$$

where $r_0 = 2.82 \times 10^{-13}$ cm is the classical electron radius and f=0.337is the transition oscillator strength. Thus the photon absorption cross section can be described by Lorentzian lineshape:

$$\sigma(\nu) = fr_e c \frac{\frac{\Gamma_A}{2}}{(\nu - \nu_0)^2 + (\frac{\Gamma_A}{2})^2} \tag{1.6}$$

where Γ_A is the pressure dependent FWHM, $\Gamma_A \approx 0.04 nm/amg \cdot [^3He]$. At the front of the cell, the photon spectral flux density is the product of a Gaussian spatial
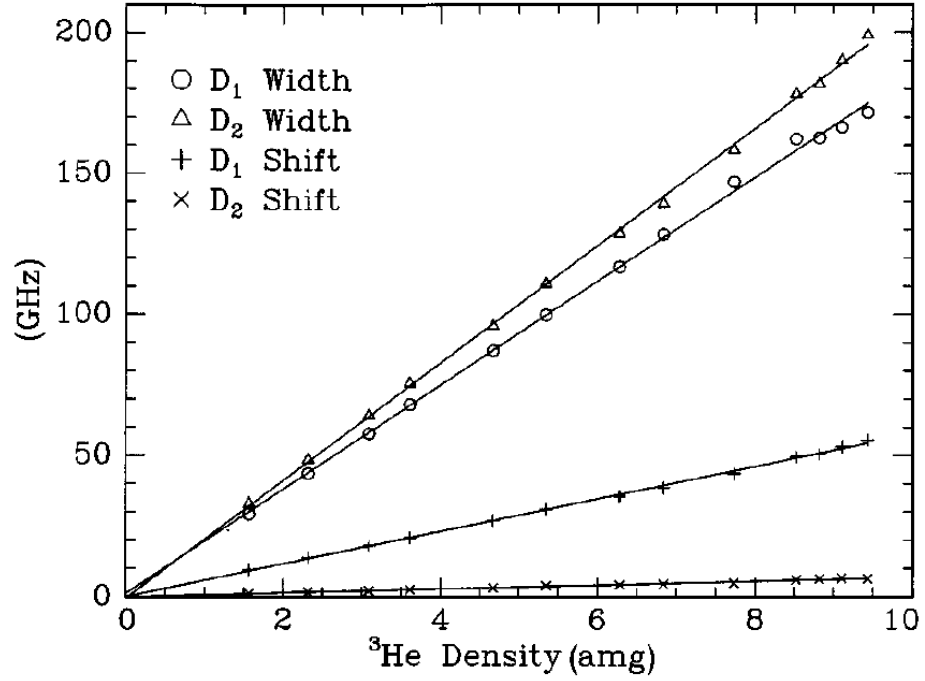
Figure 1.5: The shift and the broadening due to presence of ^{3}He for Rb D_1 and D_2 lines. (from Ref. [6])

distribution and a Gaussian spectrum.

$$\phi(\nu, \vec{r}) = \phi_0(\vec{r})G(\nu) \tag{1.7a}$$

$$\phi_0(\vec{r}) = \frac{P}{h\nu}\frac{2}{\omega^2\pi}e^{2r^2/\omega^2} \tag{1.7b}$$

$$G(\nu) = \frac{1}{\sqrt{2\pi}\sigma_l}e^{-(\nu-\nu_l)^2/2\sigma_l^2} \tag{1.7c}$$

where P is the laser power; ω is the beam waist; σ_l is the Gaussian width of the laser and ν_l is the central laser frequency.

10

1.2.6 Polarization Time Evolution

Polarizations of Rb electrons are more complex, but ^3He nuclei have an intrinsic nuclear spin of 1/2, and it is simpler to explain the math with spin of 1/2. Let's define the polarization as the asymetry between +1/2 state and -1/2 state:

$$P = \frac{\rho_{+1/2} - \rho_{-1/2}}{\rho_{+1/2} + \rho_{-1/2}} = \rho_{+1/2} - \rho_{-1/2} \tag{1.8}$$

where $\rho_{\pm 1/2}$ is the population in the $\pm 1/2$ state.

The time evolution of polarization for both Rb electrons and ^3He follows the equation:

$$\frac{dP}{dt} = \gamma(1 - P) - \Gamma \cdot P \tag{1.9}$$

γ is the polarization rate and Γ is the depolarization rate in the above differential equation. The solution has the simple form of:

$$P(t) = Ce^{-(\gamma + \Gamma)t} + \frac{\gamma}{\gamma + \Gamma} \tag{1.10}$$

Note the depolarization rate also contributes to the rate at which P approaches saturation as it lowers the saturated polarization hence shortens the time to reach it. The saturated polarization is defined as the value of P in the limit t → ∞:

$$P_\infty = \frac{\gamma}{\gamma + \Gamma} \tag{1.11}$$

The initial polarization is defined as the value of P at t = 0:

$$P_0 = C + \frac{\gamma}{\gamma + \Gamma} = C + P_\infty \tag{1.12}$$

Thus, P(t) can be expressed as:

$$P(t) = (P_0 - P_\infty)e^{-(\gamma+\Gamma)t} + P_\infty \tag{1.13}$$

In the case of polarizing Rb with a pump laser, γ is the pumping rate R and Γ is the Rb spin relaxation rate Γ_{Rb}. There is typically a small angle θ between the pump laser and the holding field even though great effort has been made to minimize the angle. Thus P(t) can be rewritten as:

$$P(t) = P_0 e^{-(R+\Gamma_{Rb})t} + P_{laser} cos\theta \frac{R}{R + \Gamma_{Rb}}(1 - e^{-(R+\Gamma_{Rb})t}) \tag{1.14}$$

θ is called the skew angle, P_{laser} is the circular polarization of the pump laser which is above 99.5%. Rb close to the front side of the cell can reach above 97% (depends on the laser power and other factors) on the order of 100's of microseconds. As the laser propagates through the cell, power is attenuated by Rb vapor. Therefore Rb polarization at the back side of the cell is lower than that at the front side. One way to overcome the problem is to shine pump laser from both sides of the cell which would lead to higher overall Rb polarization and ^{3}He polarization.

Spins are thermally polarized with the presence of a magnetic field even without external pumping source. The probability for a spin to be in state s is:

$$Prob. = \frac{e^{-E_s/k_B T}}{\sum_{si} e^{-E_{si}/k_B T}} \tag{1.15}$$

where E_s is the energy of the state, k_B is the Boltzmann constant and T is the temperature. Using the thermal distribution, under typical operating conditions, ^3He polarization is 10^{-9} and Rb polarization is 10^{-5}. Both are negligible without active

pumping.

1.2.7 Rb Spin Destruction Rate

There are two main mechanisms of Rb depolarization: the binary collisions with Rb, ^{3}He and N_2, and the formation and breakup of van der Waals molecules, the second mechanism is negligible for ^{3}He cells. The Rb spin destruction rate can then be expressed as

$$\Gamma_{Rb} = k_{Rb-Rb}[Rb] + k_{Rb-^3He}[^3He] + k_{Rb-N_2}[N_2] \tag{1.16}$$

where k_{Rb-X} is the spin destruction rate constant and $[X]$ is the density of X. Dolph has summarized these constants based on measurements from various groups:

$$k_{Rb-^3He}(T) = 55.9(9) \left(\frac{T}{473.15K} \right)^{3.31(12)} Hz/amg \tag{1.17a}$$

$$k_{Rb-N_2}(T) = 290(30) \left(\frac{T}{473.15K} \right)^{2.0(25)} Hz/amg \tag{1.17b}$$

$$k_{Rb-Rb} = 4.813(48) \times 10^{-13} Hz \cdot cm^3 \tag{1.17c}$$

For a pure Rb cell at 170°C with the following densities in the pumping chamber:

$$[^3He] \approx 8.0amg \tag{1.18a}$$

$$[N_2] \approx 0.08amg \tag{1.18b}$$

$$[Rb] \approx 6.0 \times 10^{14} cm^{-3} \tag{1.18c}$$

The approximate spin destruction rates due to various gases are:

13

$$\Gamma_{Rb-{}^3He} \approx 360 Hz \tag{1.19a}$$

$$\Gamma_{Rb-N_2} \approx 20 Hz \tag{1.19b}$$

$$\Gamma_{Rb-Rb} \approx 289 Hz \tag{1.19c}$$

The total spin destruction rate is 669 Hz. With more than 20 W narrowband laser, the optical pumping rate is often 100s kHz, which is much greater than the total Rb spin destruction rate. Therefore, it is very easy to achieve a close to unity alkali polarization.

1.3 Spin Exchange

Following equation 1.14, the time evolution of ^3He polarization can be expressed as:

$$P_{{}^3He}(t) = P_0 e^{-(\gamma_{se}+\Gamma)t} + P_{Rb}\frac{\gamma_{se}}{\gamma_{se}+\Gamma}(1 - e^{-(\gamma_{se}+\Gamma)t}) \tag{1.20}$$

The saturation polarization is

$$P_\infty = P_{Rb}\frac{\gamma_{se}}{\gamma_{se}+\Gamma} \tag{1.21}$$

where γ_{se} is the spin exchange rate between ^{3}He and Rb, and Γ is the spin relaxation rate.

1.3.1 Spin-Dependent Interactions

The key process in spin-exchange optical pumping is collisional transfer of polarization between optically pumped alkali-metal atoms and the nuclei of the noble gas atoms.

As in Fig. 1.6, the transfer of angular momentum occurs either while the atoms are bound in van der Waals molecules or in simple binary collisions. For ^3He, binary collisions dominate, and the contribution from van der Waals molecules is negligible. The time scale for binary collisions is on the order of 10^{-12} sec, the collision can induce both $\Delta F = \pm 1$ and $\Delta F = 0$ transitions between hyperfine sublevels. For heavier noble gases like ^{129}Xe at pressure of a few tens of Torr, the contributions of van der Waals molecuels can greatly exceed that of binary collisions. At several atms which is the typical operating pressure for SEOP, the time scale of van der Waals molecules is greatly limited by collision so that the binary collisions dominate.

Spin-dependent interactions produce the spin transfer and relaxation. For SEOP, spin-rotation interaction between $\vec{S}$ and the rotational angular momentum $\vec{N}$ of the atom pair formed by Rb and noble gas atom, and the isotropic hyperfine interaction between $\vec{S}$ and the noble-gas nuclear spin $\vec{I_b}$ dominate the spin-exchange process:

$$V_1(\vec{R}) = \gamma(R)\vec{N} \cdot \vec{S} + A(R)\vec{I_b} \cdot \vec{S} \qquad (1.22)$$

The spin-rotation interaction is caused by the magnetic fields from relative motion of the charges of the colliding atoms, and the isotropic hyperfine interaction comes from the magnetic field inside the nucleus of the noble-gas atom. The spin-rotation interaction produces relaxation of the alkali-metal electron-spins, while the isotropic hyperfine interaction transfers angular momentum back and forth between the alkali-metal electron spins and the noble-gas nuclear spins.

An alkali-metal atom and a noble-gas atom interact via both a large spin-independent interaction $V_0(R)$ and a small spin-dependent interaction $V_1(R)$. At the high oper-
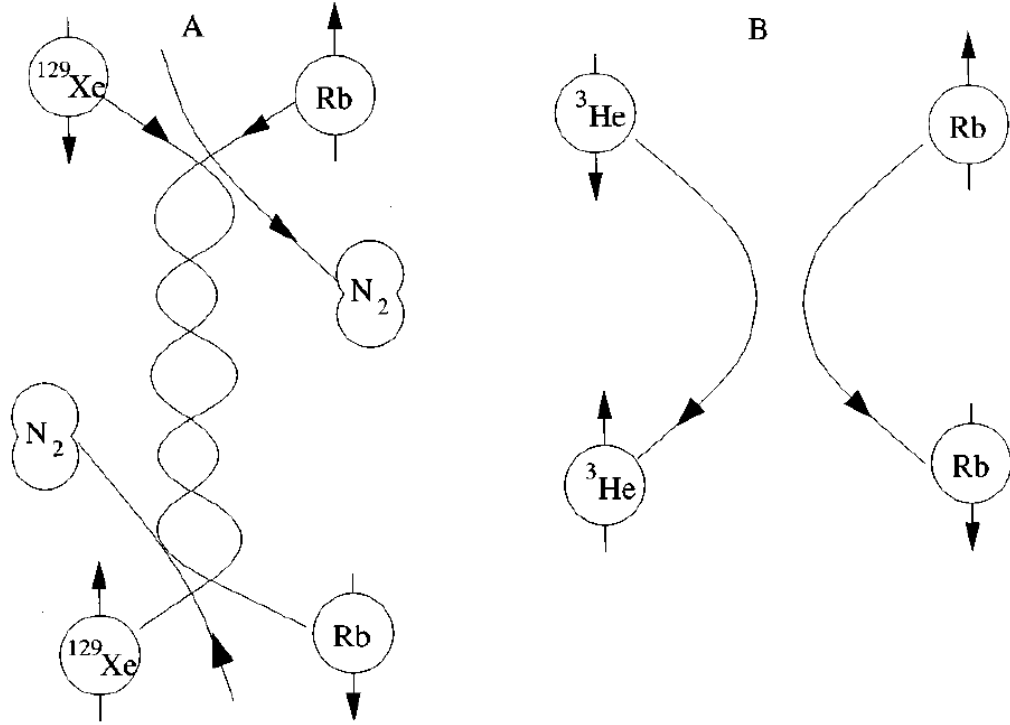
Figure 1.6: A. Formation and breakup of alkali-metal/noble-gas van der Waals molecule. B. Binary collision between an alkali-metal atom and a noble-gas atom. (from Ref. [10])

ating temperatures, V_0 determines classical collision trajectories, while V_1 acts as a small perturbation. We'll focus on V_1 below since it is responsible for spin exchange.

Including a few more terms that were neglected in Eq. 1.7, the spin-dependent interaction $V_1(R)$ can be expressed as:

$$V_1(\vec{R}) = \gamma(R)\vec{N} \cdot \vec{S} + \sum_k A_k(R)\vec{I}_k \cdot \vec{S}$$

$$+ \sum_k B_k(R)\vec{I}_k \cdot (3\vec{R}\vec{R} - 1) \cdot \vec{S} \qquad (1.23)$$

$$+ \sum_k C_k(R)\vec{I}_k \cdot (3\vec{R}\vec{R} - 1) \cdot \vec{I}_k$$
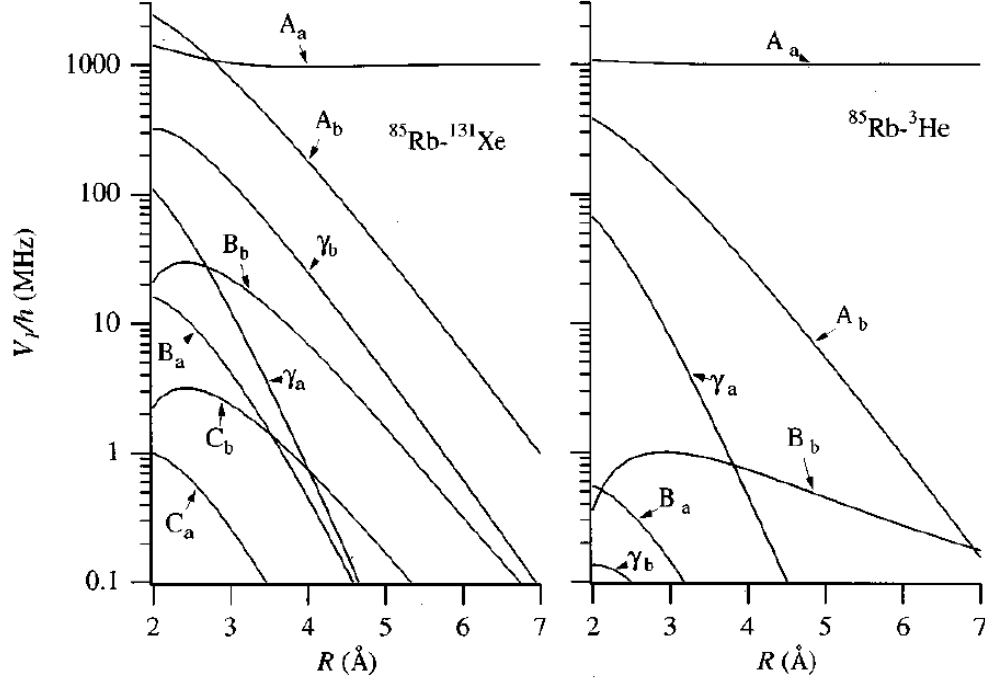
Figure 1.7: Strengths of various spin-dependent interactions as functions of separation(from Ref. [10])

where $\vec{I}_a$ and $\vec{I}_b$ are the nuclear spins of the atomic pair, where a stands for alkali metal atom and b stands for noble gas atom. γ is the coefficient of the spin-rotation interaction, while A_k, B_k, C_k are the coefficients for isotropic magnetic-

17

dipole hyperfine interactions, anisotropic magnetic-dipole hyperfine interactions, and electric quadrupole interactions, respectively. A_a greatly exceed other coefficients as the separations between atoms increase.

The isotropic hyperfine interactions come from the Fermi-contact magnetic fields of the two nuclei. A_b is the term responsible for spin exchange:

$$A_b(R) = \frac{8\pi g_s \mu_B \mu_b}{3I_b} |\eta \phi_0(R)|^2 \tag{1.24}$$

where η is the enhancement factor which equals to the ratio of the perturbed wave function at the noble gas nucleus to that without the noble gas atom. The isotropic hyperfine interaction also introduces a frequency shift of the magnetic resonance lines for alkali-metal and noble gas atoms. The frequency shift is characterized by another enhancement factor κ which is the ratio of the actual shift of the alkali metal electron lines due to the presence of polarized noble gas nuclei to what would be produced by the bulk magnetization of polarized noble gas. The shift is used in the technique Electron Paramagnetic Resonance (EPR) to calculate the polarization of noble gas nuclei.

The isotropic magnetic-dipole coupling polarizes the noble gas nuclei parallel to the electron spin polarization, while the anisotropic magnetic-dipole coupling polarizes in the opposite direction. Fortunately, the anisotropic interaction is negligible compared to isotropic interaction.

1.3.2 Spin Exchange Rate

The spin exchange rate due to binary collisions is:

$$\gamma_{se} = <\sigma_{se}v> [Rb] = k_{se}[Rb] \tag{1.25}$$

where $k_{se} = <\sigma_{se}v>$ is the velocity-averaged spin exchange rate constant. k_{se} for spin exchange between ^3He and Rb is:

$$k_{se}^{^3He-Rb} = (6.7 \pm 0.7) \times 10^{-20} cm^3/s \tag{1.26}$$

Under 170°C which is a typical temperature that we run tests with,

$$[Rb] = 2.60 \times 10^{14} cm^{-3} \tag{1.27}$$

Thus for a single chamber cell,

$$\frac{1}{\gamma_{se}} \approx 15.9 hrs \tag{1.28}$$

1.4 ^3He Spinup and Relaxation

Similar to the optical pumping process of Rb, ^3He polarization can be described by

$$P_{^3He}(t) = P_0^{^3He} e^{-(\gamma_{se}+\Gamma)t} + P_\infty^{^3He}(1 - e^{-(\gamma_{se}+\Gamma)t}) \tag{1.29}$$

where the saturation polarization is

$$P_\infty^{^3He} = P_\infty^{Rb} \frac{\gamma_{se}}{\gamma_{se} + \Gamma} \tag{1.30}$$

And Γ is the total relaxation rate of ^{3}He nucleus spin polarization,

$$\Gamma = \Gamma_{dipolar} + \Gamma_{inhomogeneity} + \Gamma_{wall} \tag{1.31}$$

When a target cell are used in electron scattering experiments where an electron beam goes through part of the cell, an additional relaxation rate due to the beam Γ_{beam} should also be included.

The coupling of nuclear spin to orbital angular momentum creates an intrinsic ^{3}He relaxation rate that depends on density. At room temperature $(23°C)$, the dipolar relaxation rate is

$$\frac{1}{\Gamma_{dipolar}} = \frac{[^3He]}{744} hr^{-1} \tag{1.32}$$

where $[^3He]$ is the ^3He density in amagats. Assuming the cell density is 8 amg, the relaxation rate is $1/93 \ hr^{-1}$. In addition, there is an additional intrinsic relaxation due to the spin-rotation interaction. This mechanism dominates the relaxation for ^{129}Xe but is small for ^{3}He.

The relaxation rate due to field inhomogeneities is

$$\Gamma_{inhomogeneity} = D\frac{|\nabla B_x|^2 + |\nabla B_y|^2}{B_0^2} \tag{1.33}$$

where D is the ^{3}He diffusion constant, ∇B_x and ∇B_y are the transverse magnetic field inhomogeneities, B_0 is the holding field along z-axis. Under operating conditions, assuming the pressure is around 12 atm and field is 12.6 G, $D \approx 0.16 cm^2/s$ and the field inhomogeneities are 10mG/cm, the relaxation rate is 1/1400 hr^{-1}.

Wall relaxation is typically the dominant relaxation mechanism for cells in our lab. This mechanism depends on the property of the inner surface of glass. Most

of the target cells are contructed with reblown General Electric Type 180 (GE-180) glass. This aluminosilicate glass is highly impermeable to ^{3}He. The wall relaxation is believed to be associated to several different mechanisms, such as paramagnetic impurities in the glass and microfissures in the surface that could trap ^{3}He atoms. It has been found reblowing the glass can help lower the wall relaxation rate because it reduces the number of microfissures. The wall relaxation is not well understood, but it is believed to scale with the surface-to-volume ratio:

$$\Gamma_{wall} = \rho S/V \tag{1.34}$$

where ρ is called relaxivity.

1.5 X Factor

In 2006, Babcok *et al.* reported evidence of a previously unrecognized spin relaxation mechanism, and named it X factor. This mechanism appears to be temperature dependent and roughly proportional to alkali density. The X factor limits the maximally achievable ^{3}He polarization even with infinite laser power. The saturation polarization is

$$P_\infty^{^3He} = P_\infty^{Rb} \frac{\gamma_{se}}{\gamma_{se}(1 + X) + \Gamma} \tag{1.35}$$

In the presence of infinite laser power where $\gamma_{se} \gg \Gamma$, the saturation polarization becomes

$$P_\infty^{^3He} = P_\infty^{Rb} \frac{1}{1 + X} \tag{1.36}$$

21

Chapter 2

^{3}He Polarimetry

2.1 Overview

Traditional pure glass target cells are studied mainly using Adiabatic Fast Passage (AFP) Nuclear Magnetic Resonance (NMR) and Electron Paramagnetic Resonance (EPR). AFP is a technique that allows us to monitor a signal that is directly proportional to the ^{3}He polarization, which serves as a means to gain knowledge of properties of cell including the time it takes to polarize it and the relaxation rates of its polarization. The EPR technique utilizes the fact that polarized ^{3}He produces frequency shift of the magnetic resonance lines of alkali metal to measure the ^{3}He polarization. When AFP and EPR are combined, we can calculate the calibration constant between an AFP signal and the corresponding ^{3}He polarization.

A significant focus of my studies is on exploring cells that incorporate metal. Unfortunately, AFP is not suitable for studying these cells as it requires exposing the entirety of the cell to a Radio Frequency (RF) magnetic field in an attempt to flip all

spins in the cell. The RF field would induce an Eddy current induced in the metal body that significantly affects the resulting signal. For these cells, Pulsed Nuclear Magnetic Resonance (PNMR) has proven to be very useful. PNMR only applies a pulsed RF field to a small selected part of the cell which makes it relatively easy to prevent metal from distorting the signal. However, the spins tipped by applying the pulse lose their transverse component (which depends on the "tip angle"), we typically allow some time for this portion of gas to diffuse out of the region being monitored before we can the next measurement on a fresh sample of the gas. The highest rate at which PNMR measurements can be taken is limited by this requirement.

This chapter introduces the three techniques mentioned above and how they're used for our studies.

2.2 Adiabatic Fast Passage

2.2.1 Nuclear Magnetic Resonance

The energy of a magnetic moment in an external field is

$$E = -\vec{\mu} \cdot \vec{B_0} = -\mu_z B_0 \tag{2.1}$$

where $\vec{\mu}$ is the magnetic moment, for a spin-1/2 nuclei, the energy is

$$E = -\gamma B_0 \hbar/2 \tag{2.2}$$

γ is the gyromagnetic ratio, $\gamma/2\pi \approx 3.2434 kHz/Gauss$. When a oscillating magnetic field with the frequency $\omega = \gamma B_0$ is present, transitions between the $+1/2$ and

-1/2 states are induced. This frequency is called Larmor frequency. When a nucleus is placed in an external magnetic field that is not aligned with its magnetic moment, it will precess at the Larmor frequency.

2.2.2 The Rotating Coordinate System

2.2.2.1 Classical Formulation

For a nucleus in an external field $\vec{B}$ with $\gamma\hbar\vec{I}$ as its nuclear angular momentum, the equation of motion in a stationary coordinate system is [7]

$$\hbar\frac{d\vec{I}}{dt} = \gamma\hbar\vec{I} \times \vec{B} \tag{2.3}$$

Let $\frac{\partial}{\partial t}$ represent the derivative with respect to a coordinate system that rotates with angular velocity $\vec{\omega}$,

$$\frac{d\vec{I}}{dt} = \frac{\partial\vec{I}}{\partial t} + \vec{\omega} \times \vec{I} \tag{2.4}$$

Substitute Eq. 2.4 into Eq. 2.3, $\vec{I}$ in the rotating frame satisfies the equation of motion

$$\hbar\frac{\partial\vec{I}}{\partial t} = \gamma\hbar\vec{I} \times (\vec{B} + \vec{\omega}/\gamma) = \gamma\hbar\vec{I} \times \vec{B_{eff}} \tag{2.5}$$

where $\vec{B_{eff}}$ is the effective field in the rotating frame

$$\vec{B_{eff}} = \vec{B} + \vec{\omega}/\gamma \tag{2.6}$$

Thus, the effective field experienced by an observer in the rotating frame is simply the external field $\vec{B}$ plus an additional field $\vec{\omega}/\gamma$.

If we apply this result to rotating magnetic fields, we will get the core idea of performing an Adiabatic Fast Passage (AFP) measurement. Assuming a constant field $\vec{B}$ and another field $\vec{B_1}$ perpendicular to $\vec{B}$ that is rotating with angular velocity $-\omega$. In the rotating frame that rotates with $\vec{B_1}$, both aforementioned fields are just constant and the effective field in the rotating frame is

$$B_{eff}\vec{z} = (B - \omega/\gamma)\vec{z} + B_1\vec{x'} \tag{2.7}$$

where $\vec{x'}$ is the direction that $\vec{B_1}$ is in. When on resonance (B $= \omega/\gamma$), the effective field is perpendicular to the constant field $\vec{B}$.

2.2.2.2   Quantum Mechanical Formulation

The above conclusion can be easily reached with quantum mechanics. The Shrödinger equation for a magnetic moment in an external field is

$$i\hbar\dot{\psi} = \mathcal{H}\psi = -\gamma\hbar\vec{I} \cdot \vec{B}\psi \tag{2.8}$$

Let ψ and $\vec{B}$ be the wave function and magnetic field in a stationary frame and ψ_r and $\vec{B_r}$ be the same quantities in a rotating frame with angular velocity $\vec{\omega}$. Using the rotation operator in quantum mechanics,

$$\psi = e^{-i\vec{\omega}\cdot\vec{I}t}\psi_r \tag{2.9a}$$

$$\vec{I} \cdot \vec{B_r} = e^{i\vec{\omega}\cdot\vec{I}t}\vec{I} \cdot \vec{B}e^{-i\vec{\omega}\cdot\vec{I}t} \tag{2.9b}$$

Substituting 2.9 into Eq.2.8, the Shrödinger equation in the rotating frame is obtained

$$i\hbar\dot{\psi}_r = -\gamma\hbar\vec{I} \cdot (\vec{B}_r + \vec{\omega}/\gamma)\psi_r = -\gamma\hbar\vec{I} \cdot \vec{B}_{eff}\psi_r \tag{2.10}$$

The same effective field in the rotating frame is reached as that from the classical derivation.

2.2.3 Adiabatic Fast Passage

Adiabatic Fast Passage (AFP) NMR is used to measure the ^{e}He polarization. In an AFP measurement, with the assistance of a oscillating radiofrequency (RF) field, the spins follow the effective field in a rotating frame (as discussed in more detail below) and are flipped 180 degrees to the opposite direction and then flipped back, producing two peaks in signal when they're perpendicular to the holding field and the pick up coils.
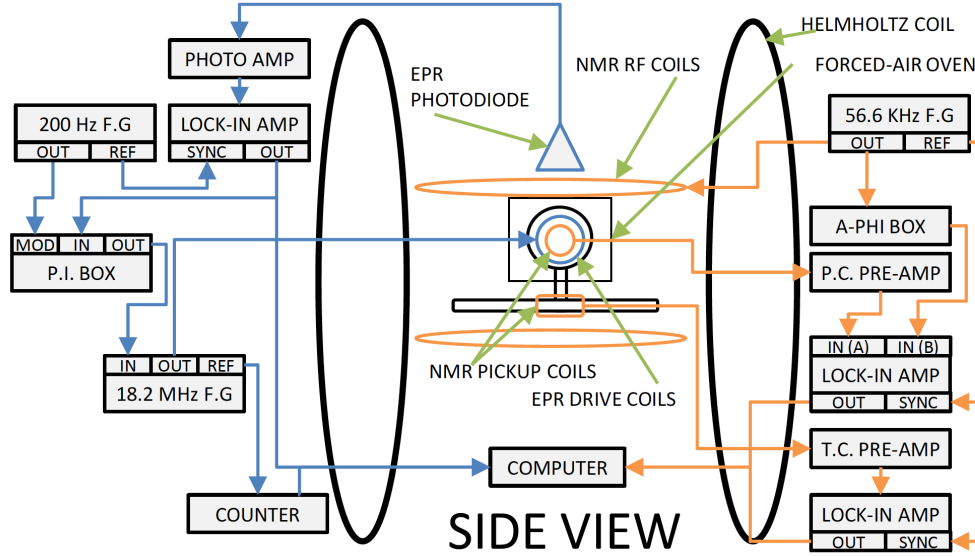
Figure 2.1: EPR (left) and AFP (right) setup. Adapted from Dolph's PhD thesis.

The flipping process can be achieved by either sweeping the main holding field or sweeping the RF frequency so that the longitudinal component of effective field in the rotating frame goes through zero. AFP measurements in out lab are typically done by sweeping the holding field while keeping the RF frequency constant. The RF coils produce a RF field of magnitude $2B_1$ perpendicular to the main holding field B. The oscillating field has a frequency of ω and can be decomposed into two counter-rotating components with the same amplitude B_1. Only the component rotating in direction able to give a resonance in Eq. 2.7 has an important effect. In this frame, the effective field is

$$B_{eff}\vec{z} = (B - \omega/\gamma)\vec{z} + B_1\vec{x'} \tag{2.11}$$

27

as discussed above. The other rotating component that rotates in the opposite direction does not affect the spins. In an AFP measurement, the holding field starts from a value lower than ω/γ ($\omega/\gamma - B \gg B_1$), so that the effective field is almost aligned with the holding field and the spins. The holding field is then swept at a constant rate through resonance to a value greater than ω/γ. The sweeping rate is of great importance. The sweep needs to be slow enough so that the nuclear spins can follow the effective field

$$\frac{\dot{B}}{B_1} \ll \omega \tag{2.12}$$

Sweep that satisfies this condition is considered as adiabatic.

Sweep rate cannot be too slow either, because the relaxation rate of the spins are faster near the resonance especially with a small effective field B_1. The relaxation rate of ^{3}He in the rotating frame at resonance is

$$\frac{1}{T_{1r}} = D\frac{|\nabla B_z|^2}{B_1^2} \tag{2.13}$$

where D is the ^{3}He self-diffusion constant. In order to keep the AFP loss low, it's important for the time scale that the spins stay close to resonance to be much shorter than $1/T_{1r}$:

$$D\frac{|\nabla B_z|^2}{B_1^2} \ll \frac{\dot{B}}{B_1} \tag{2.14}$$

Typically, the field is swept from 12.6 Gauss to 20.4 Gauss in 6s, thus

$$\dot{B} = 1.3G/s \tag{2.15a}$$

$$B1 \approx 100mG \tag{2.15b}$$

$$f = 56.6kHz \tag{2.15c}$$

$$D \approx 0.16cm^2/s \tag{2.15d}$$

$$|\nabla B_z| \approx 10mG/cm \tag{2.15e}$$

$$\tag{2.15f}$$

With these operating conditions,

$$D\frac{|\nabla B_z|^2}{B_1^2} \approx 1.6mHz \tag{2.16a}$$

$$\frac{\dot{B}}{B_1} \approx 13Hz \tag{2.16b}$$

$$w \approx 356kHz \tag{2.16c}$$

The AFP conditions are clearly well satisfied. Fig.2.2 shows the evolution of effective field in the rotating frame during an AFP measurement.
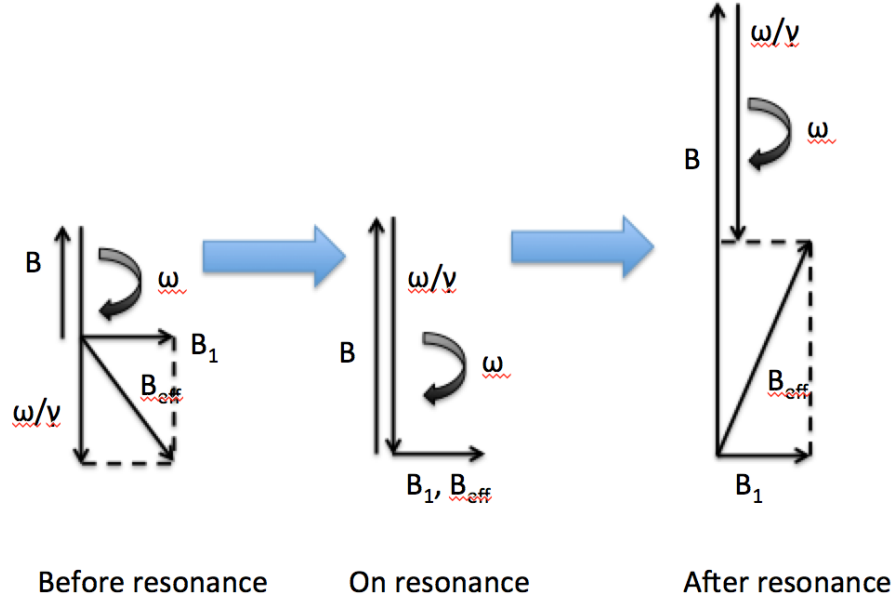
Figure 2.2: Effective field in the rotating frame during an Adiabatic Fast Passage measurement. The ^3He spins follow the direction of the effective field. B_1 is exaggerated to show different components of effective field clearly.

The pick up coils are placed close to the cell and perpendicular to the holding field and RF field. As the ^{3}He spins precess along the holding field, the transverse component of the spins will induce an electromotive force (EMF) that is directly proportional to the amplitude of the component in the pick up coils. The signal can be written as:

$$S = A\omega \sin\alpha(t) = A\omega \frac{B_1}{\sqrt{B_1^2 + (B(t) - \omega/\gamma)^2}} \tag{2.17}$$

where A is a constant that accounts for the cell and coils geometry, the cell magnetization and the electronics factors that affect the size of signal; ω is the RF frequency; α is the angle between the effective field and the holding field in the rotating frame; B(t) is the holding field as a function of time. The signal reaches peak value when $B(t) = \omega/\gamma$. Fig.2.3 shows the result of a typical AFP measurement.
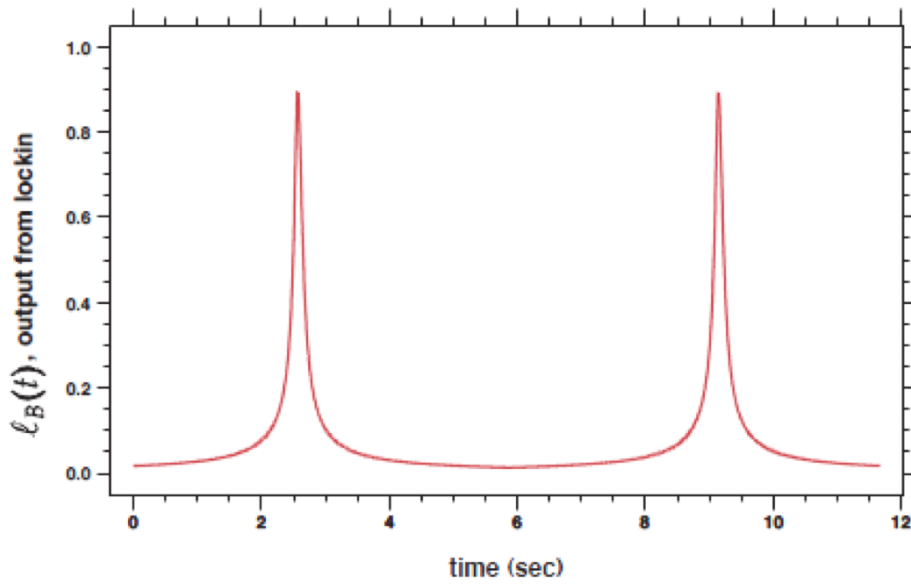
Figure 2.3: A typical AFP signal. y axis is in arbitrary unit.

2.2.4 Spinups and Spindowns

As previously mentioned, AFP is used to monitor the polarization of ^{3}He. An exact value of polarization remains to be calibrated with EPR, but the signal size is directly proportional to the polarization, thus is an indication of how the polarization changes relatively. Two processes that are monitored with AFP are spinups and spindowns.

31

2.2.4.1 Double-Chambered Cell Spinup

The process of ^{3}He gaining polarization through spin-exchange with Rb that is being constantly pumped by circularly polarized laser is called a spinup. The equation that describes spinups of single-chambered cell was already discussed in Chapter 2. But target cells used in electron-scattering experiments are normally composed of two chambers: a pumping chamber (PC), which is placed in an oven and pumped by circularly polarized laser, and a target chamber (TC) that the electron beam passes through. Fig.3.2 shows a typical cell.
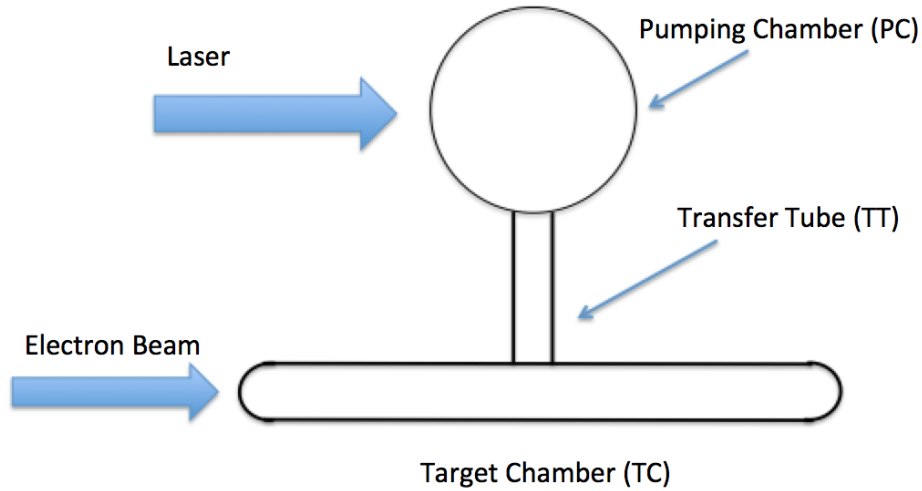
Figure 2.4: A target cell. The dimensions of different parts of the cell are not to scale.

As only the ^{3}He nuclei in the pumping chamber are gaining polarization and the electron beam constantly causes additional relaxation in the target chamber, it is im-

portant that the ^{3}He from PC can replenish the polarization in TC quickly enough. Before the 12GeV upgrade of JLab, this was normally achieved through diffusion. With higher electron beam after the upgrade, it is currently the plan that design of future cells will be changed. The number of transfer tubes will be increased to two with one of them being heated causing a temperature gradient between the two transfer tubes and driving controllable convection. This new design is called convection cell and is discussed thoroughly by Dolph. The following derivation will only focus on the old design with diffusion for simplicity. The polarization accumulation process can be described by

$$\frac{dP_{PC}}{dt} = \gamma_{se}(P_A - P_{PC}) - \Gamma_{PC}P_{PC} - d_{PC}(P_{PC} - P_{TC}) \tag{2.18a}$$

$$\frac{dP_{TC}}{dt} = -\Gamma_{TC}P_{TC} + d_{TC}(P_{PC} - P_{TC}) \tag{2.18b}$$

where $P_{PC}(P_{TC})$ is the ^{3}He polarization in PC (TC); γ_{se} is the spin-exchange rate in PC; $\Gamma_{PC}(\Gamma_{TC})$ is the relaxation rate o ^{3}He polarization in PC (TC); $d_{PC}(d_{TC})$ is the probability for a nucleus to leave PC (TC) and enter TC (PC). The transfer rates d_{PC} and d_{TC} are related by:

$$f_{PC}d_{PC} = f_{TC}d_{TC} \tag{2.19}$$

where $f_{PC}(f_{TC})$ is the fraction of atoms in PC (TC). The solutions to Eq.2.18 are

$$P_{PC}(t) = C_{PC}e^{-\gamma_f t} + (P_{PC}^0 - P_{PC}^\infty - C_{PC})e^{-\gamma_s t} + P_{PC}^\infty \tag{2.20a}$$

$$P_{TC}(t) = C_{TC}e^{-\gamma_f t} + (P_{TC}^0 - P_{TC}^\infty - C_{TC})e^{-\gamma_s t} + P_{TC}^\infty \tag{2.20b}$$

Detailed discussion is done by Dolph**??**. It's interesting to note the time evolution of ^{3}He polarization for double-chambered cells has two time constant: the fast time constant γ_f that is dominated by the diffusion rates d_{PC} and d_{TC} when diffusion is relatively fast, and the slow time constant γ_S that is mostly determined by the volume averaged spin-exchange rate. In the fast-transfer limit, double-chambered solution reduces to single-chambered solution.

The other interesting point is the relation between the saturation polarization in PC and TC

$$P_{TC}^{\infty} = \frac{P_{PC}^{\infty}}{1 + \frac{\Gamma_{TC}}{d_{TC}}} \tag{2.21}$$

Again, in the fast-transfer limit where $d_{TC} \gg \Gamma_{TC}$, $P_{TC}^{\infty} = P_{PC}^{\infty}$. Fig. 2.5 shows an example of spinup curves for a double-chambered cell. This spinup is different than regular ones in that the AFP measurements were taken every 3 minutes (normal sample rate is one AFP every one hour), thus the losses due to frequent measurements limited the saturation polarization. The raw signal obtained from AFP have already been calibrated by EPR so the y axis is polarization rather than raw signal amplitude.
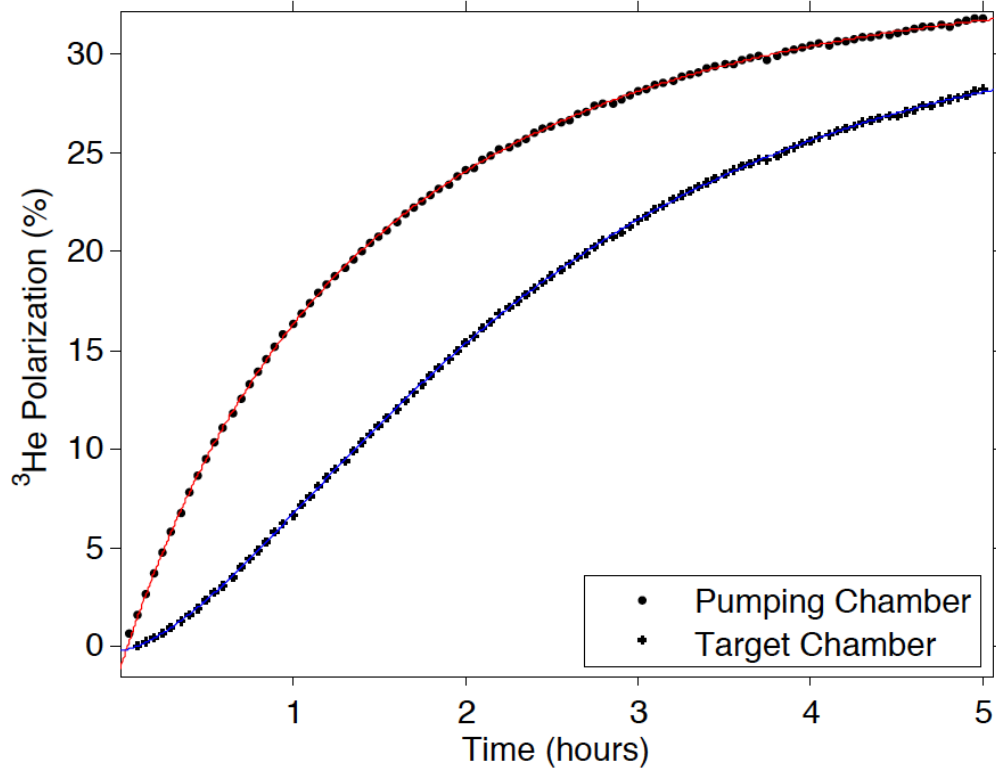
Figure 2.5: ^{3}He polarization as a function of time for both the pumping chamber and the target chamber. The top curve is the pumping chamber and the bottom curve is the target chamber.

2.2.4.2 Initial Spinup

As shown in Fig.2.5, the early spinup behaviors of the pumping chamber and the target chamber are quite different. The initial part of the pumping chamber is almost linear but the target chamber shows a curved initial part. By performing a Taylor expansion on Eq. 2.20 we obtain the initial part of the spinup for both chambers:

$$P_{PC}(t) = \gamma_{se}P_At - \frac{1}{2}\gamma_{se}P_A(\gamma_{se} + \Gamma_{PC} + d_{PC})t^2 \qquad (2.22\text{a})$$

$$P_{TC}(t) = \frac{1}{2}\gamma_{se}P_Ad_{TC}t^2 \qquad (2.22\text{b})$$

where γ_{se} is the spin-exchange rate in the pumping chamber and P_A is the alkali polarization. It's clear that the dominant term in $P_{PC}(t)$ is the linear term while the shape of $P_{TC}(t)$ is quadratic.

The slope of the linear shape of initial spinup of the pumping chamber gives access to the product $P_A\gamma_{se}$ and fitting the initial spinup of the target chamber to a quadratic function provides the product $\gamma_{se}P_Ad_{TC}$. The alkali polarization P_A can be measured with a technique named Faraday Rotation, we then gain knowledge of the spin-exchange rate γ_{se} and the diffusion rate d_{TC}.

2.2.4.3 Spindown

The spin relaxation rates in the pumping chamber and the target chamber are different due to geometric and other properties. The cell-average relaxation rate can then be written as

$$\langle\Gamma\rangle = f_{PC}\Gamma_{PC} + f_{TC}\Gamma_{TC} \qquad (2.23)$$

where f_{PC} (f_{TC}) is the fraction of atoms in PC (TC); Γ_{PC} (Γ_{TC}) is the average relaxation rate in PC (TC). When the cell is being pumped by laser, the pumping chamber is heated with hot air to create alkali vapor while the target chamber remains at the room temperature. Difference in temperature further complicates difference in relaxation rates between the two chambers. However, when trying to measure the

life time (the inverse of the relaxation rate) of the cell, we typically keep the entire cell at room temperature and perform a "spindown" measurement.

During a spindown, the cell starts with some polarization (normally as high as possible so we can obtain a more complete curve), and relaxes on its own while we take AFP measurements at a certain rate. Typically, the interval between measurements is anywhere between 30 mins and 2 hrs, depending on the lifetime of the cell. The rule of thumb is to take AFP frequently enough so the spindown curve has sufficient data points while not too often so the polarization relaxes too fast due to AFP losses. The ^{3}He polarization relaxation can be described by

$$P(t) = P_0 e^{-t/\tau_{true}} \tag{2.24}$$

The true lifetime τ_{true} of the cell without relaxation due to AFP loss can be measured with two methods: the first is to take 5 AFP measurements consecutively with very short interval (normally around 3 minutes), the second is to perform several spindown measurements, each with a different interval.

In the first method, because the lifetime of the cell is much longer than 3 minutes, we can safely attribute all losses to AFP measurements and extract the loss due to a single AFP $loss_{afp}$. The data values can then be corrected with the equation

$$S_i^{corrected} = S_i^{raw}/(1 - loss_{afp})^{i-1} \tag{2.25}$$

where $S_i^{corrected}$ is the corrected signal, S_i^{raw} is the raw signal, i represents it is the ith measurement in the spindown, $loss_{afp}$ is the loss due to a single measurement. Fitting the corrected values to Eq. 2.24 gives the true lifetime τ_{true}.

A simple example for the second method would be to perform one spindown with one-hour interval and another spindown with two-hour interval, the relaxation rates in these two spindowns are

$$\frac{1}{\tau_{1hr}} = \frac{1}{\tau_{true}} + \Gamma_{AFP\_1hr} \tag{2.26a}$$

$$\frac{1}{\tau_{2hr}} = \frac{1}{\tau_{true}} + \Gamma_{AFP\_2hr} \tag{2.26b}$$

$$\Gamma_{AFP\_1hr} = 2 \times \Gamma_{AFP\_2hr} \tag{2.26c}$$

where τ_{1hr} and τ_{2hr} are the lifetimes measured with taking AFP every 1 hour and every 2 hours, τ_{true} is the true lifetime of the cell without interference from measurements, Γ_{AFP_1hr} (Γ_{AFP_2hr})is the relaxation rate due to taking measurements every 1hr (2hr). We can then solve for τ_{true}.

2.2.5 AFP Loss

The longitudinal spin relaxation rate due to static field inhomogeneities is

$$\frac{1}{T_1} = D\frac{|\nabla B_x|^2 + |\nabla B_y|^2}{B_0^2} \tag{2.27}$$

where D is the diffusion constant for the polarized spins, and is inversely proportional to the gas pressure. B_0 is the mean magnetic field along z axis. B_x and B_y are the x and y components of the magnetic field. However, when performing AFP measurement, the spins are exposed to a small oscillating RF field, the spin relaxation can be greatly accelerated under magnetic resonance conditions [5],

$$\frac{1}{T_{r1}} = \frac{8R^4}{175D}|\nabla\Omega_z|^2 \sum_n \frac{175}{4(\chi_{1n}^2 - 2)(\chi_{1n}^4 + r^2 + r^2s^2)(1 + s^2)} \tag{2.28}$$

where R is the cell radius, D is the diffusion constant, Ω_z is the Larmor frequency of the holding field, $r = \frac{\omega_r R^2}{D}$, $s = \frac{\Omega_0 - \omega}{\omega_r}$, the numbers χ_{1n} are the zeros of the derivatives of the spherical Bessel functions

$$\frac{d}{dx}j_1(x_{1n}) = 0 \ for \ n = 1, 2, 3...$$ (2.29)

Since $r^2 \gg \chi_{1n}^4$, and $\sum_n \frac{1}{\chi_{1n}^2 - 2} = \frac{1}{2}$ [4],

$$\frac{1}{T_{r1}} = \frac{R^4 |\nabla \Omega_z|^2}{r^2 (1 + s^2)^2 D} = \frac{|\nabla B_z|^2 D}{B^2 (1 + s^2)^2}$$ (2.30)

If P_0 is the polarization before AFP, the polarization P after a single AFP flip is given by

$$P = P_0 e^{-\int \Gamma_{r1} dt} = P_0 e^{-\int \frac{1}{T_{r1}} dt}$$ (2.31)

Given the field sweep starts from 12.6G, ends at 20.4G, the RF frequency is 56.6kHZ, the sweep time is 6s and B_1 is 100mG, we can safely approximate the integral by

$$\int_{-\infty}^{\infty} \frac{1}{T_{r1}} dt = \frac{\pi D |\nabla B_z|^2}{2 B_1 \partial B_1 / \partial t}$$ (2.32)

which is the fractional loss due to a single AFP flip.

To better understand AFP loss, we performed a study where we took AFP measurements at various different field gradients to study the relation between AFP loss and inhomogeneities. The gradients were produced by Maxwell-style transverse gradient coils and increased from 0 to a little under 160 mG/cm. At each set gradient, we take one AFP to look at the difference between the two peaks to determine the

loss due to a single flip. Fig 2.6 shows AFP losses collected from experiments and theoretical predictions. They agree mostly within the error bar.
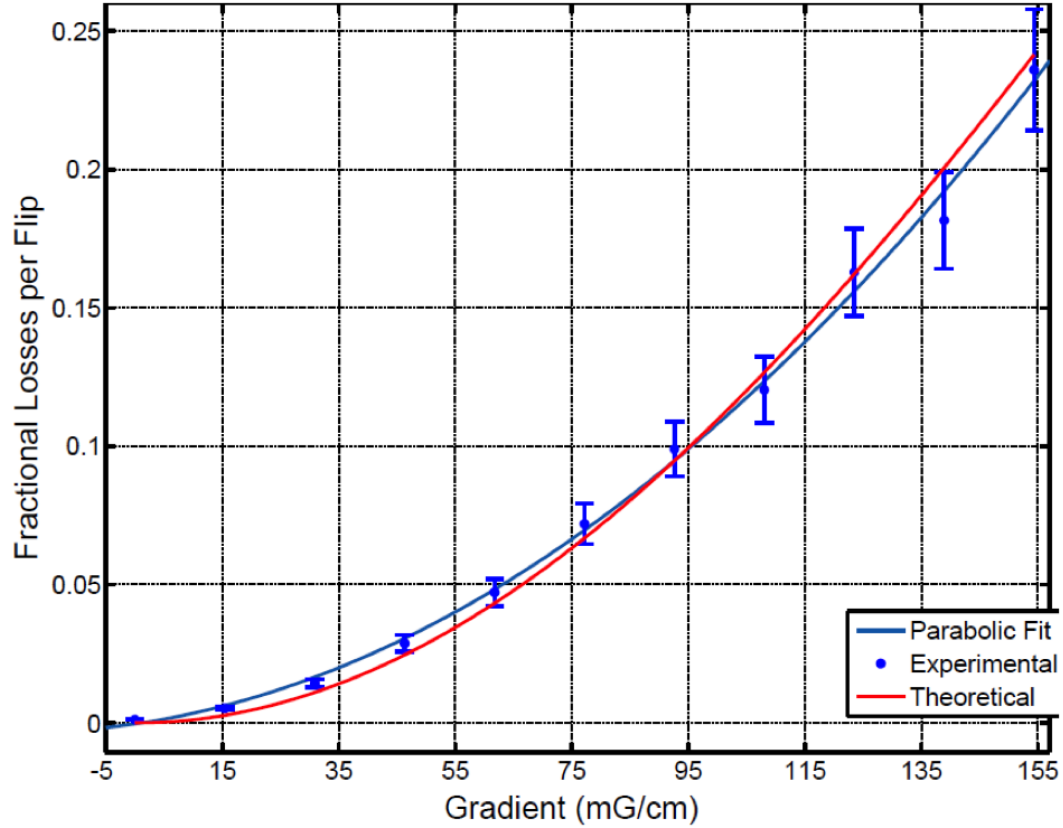
Figure 2.6: Fractional AFP loss (single flip) as a function of field gradient.

2.3 Electron Paramagnetic Resonance

2.3.1 Overview

Electron Paramagnetic Resonance (EPR) is a important technique for measuring the frequency shift of alkali metal Zeeman resonance due to the effective magnetic field produced by polarized ^{3}He gas. The EPR shift is largely caused by the Fermi-contact

interaction $\alpha\ \mathbf{K} \cdot \mathbf{S}$ between the nuclear spin $\mathbf{K}$ of the noble gas nucleus of magnetic moment μ_K and the electron spin $\mathbf{S}$ of the alkali metal atom [2]. The magnetic field created by the bulk magnetization of the ^{3}He gas also contributes directly to a relatively small part of the shift (rougly 1/6 for K). The total measured shift is therefore written as the expected Zeeman interaction with the field produced by the polarized ^{3}He multiplied by an enhancement factor κ_0. The enhancement effect comes from overlapping of alkali metal electrons and ^{3}He nuclei during binary collisions, thus κ_0 is different for each alkali metal species and slightly temperature dependent.

During the process of optical pumping, the Rb atoms are excited to the $5\mathrm{P}_{\frac{1}{2}}$ state by the pump laser. The majority of these atoms are quenched non-radiatively to the ground state by N_2. While at $5\mathrm{P}_{\frac{1}{2}}$ state, Rb atoms can also be excited to the $5\mathrm{P}_{\frac{3}{2}}$ state through collisions with other Rb atoms. A small fraction of the excited atoms $(5\mathrm{P}_{\frac{1}{2}}$ and $5\mathrm{P}_{\frac{3}{2}})$ decay by emitting either a D_1 photon or D_2 photon. The intensity of fluorescence is proportional to the excited Rb atoms, thus is higher when the Rb polarization is low so more Rb atoms can absorb laser and jump to the excited state. We typically induce Zeeman transitions with a RF coil to lower alkali polarization and detect D_2 photons with a photodiode behind a D_2 filter. The highest amount of D_2 photons is detected when the RF frequency is exactly equal to the Zeeman transition frequency.

2.3.2   The Breit-Rabi Equation

The Zeeman energy levels of ground state (L = 0) can be described with the Breit-Rabi equation

$$E_{F=I\pm 1/2,m_F} = -\frac{h\Delta\nu_{hfs}}{2(2I+1)} - \mu_N g_I B m_F \pm \frac{h\Delta\nu_{hfs}}{2}\sqrt{1 + \frac{4m_F x}{2I+1} + x^2} \qquad (2.33)$$

where

$$x = (g_I\mu_N - g_s\mu_B)\frac{B}{h\Delta\nu_{hfs}} \qquad (2.34)$$

B is the magnetic field, $\Delta\nu_{hfs}$ is the hyperfine splitting frequency, I is the nuclear spin, g_I and g_s are the g factors of nuclear and electron spin, μ_N and μ_B are the nuclear and Bohr magneton, respectively.

The Zeeman transition frequency of $m_F \to m_F - 1$ is

$$\begin{aligned}
\nu_{m_F \to m_F - 1} &= \frac{E_{F,m_F} - E_{F,m_F-1}}{h} \\
&= -\frac{g_I\mu_N B}{h} \pm \frac{\Delta\nu_{hfs}}{2}\left(\sqrt{1 + \frac{4m_F}{2I+1}x + x^2} - \sqrt{1 + \frac{4m_F - 1}{2I+1}x + x^2}\right)
\end{aligned}$$

$$(2.35)$$

The second term is much greater than the first term under our operating conditions, so the sign of the frequency $\nu_{m_F \to m_F-1}$ depends on the second term only. If we focus on the top hyperfine manifold in the energy level graph, the transition frequency is

$$\nu_{m_F \to m_F - 1} = -\frac{g_I\mu_N B}{h} + \frac{\Delta\nu_{hfs}}{2}\left(\sqrt{1 + \frac{4m_F}{2I+1}x + x^2} - \sqrt{1 + \frac{4m_F - 1}{2I+1}x + x^2}\right)$$

$$(2.36)$$

2.3.3 Shift of Zeeman Frequency

Under our operating condition, the size of Zeeman splitting is much less than hyperfine splitting, which makes x a small number. The Taylor expansion of Eq. 2.36 is

$$
\begin{aligned}
\nu_{m_F \to m_{F-1}} = & -\frac{g_I \mu_N B}{h} \\
& + \frac{\Delta\nu_{hfs}}{2}\left(\frac{2x}{2I+1} - \frac{2(2m_F-1)x^2}{(2I+1)^2} + \frac{(-(2I+1)^2 + 4 - 12m_F + 12m_F^2)x^3}{(2I+1)^3} + \cdots\right)
\end{aligned}
$$

$$(2.37)$$

With the approximation

$$g_s\mu_B \gg g_I\mu_N \tag{2.38a}$$

$$x \approx -\frac{g_s\mu_B B}{h\Delta\nu_{hfs}} \tag{2.38b}$$

To the lowest order approximation, the shift of $\nu_{m_F \to m_{F-1}}$ due to a small effective field ΔB ($\Delta B \ll B$) from polarized ^{3}He is

$$
\begin{aligned}
\Delta\nu_{m_F \to m_{F-1}} = & -\frac{g_s\mu_B}{h(2I+1)}\Delta B\left[1 + 2(2m-1)\frac{g_s\mu_B B}{h\Delta\nu_{hfs}(2I+1)}\right. \\
& + 6\left(-\frac{(2I+1)^2}{4} + 1 - 3m + 3m^2\right)\left(\frac{g_s\mu_B B}{h\Delta\nu_{hfs}(2I+1)}\right)^2 + \cdots \bigg]
\end{aligned}
$$

$$(2.39)$$

Usually the pumping chamber is spherical, the magnetic field produced inside a uniformly magnetized sphere is

$$\boldsymbol{\Delta B} = \frac{2}{3}\mu_0\boldsymbol{M} \tag{2.40}$$

43

where μ_0 is the vacuum permeability, $\boldsymbol{M}$ is the magnetization of ^{3}He,

$$\boldsymbol{M} = \boldsymbol{\mu_K}[He]P \tag{2.41}$$

where μ_K is the magnetic moment of ^{3}He, [He] is its density, and P its polarization. As we mentioned before, as a result of the Fermi-contact interaction $\alpha\mathbf{K}\cdot\mathbf{S}$ between the nuclear spin $\mathbf{K}$ of the noble gas nucleus and the electron spin $\mathbf{S}$ of the alkali metal atom, the effective magnetic field from the polarized ^{3}He gas is enhanced by a factor of κ_0:

$$\Delta\boldsymbol{B} = \frac{2}{3}\kappa_0\mu_0\boldsymbol{\mu_K}[He]P \tag{2.42}$$

The enhancement factor κ_0 was measured by Romalis *et al.* in 1998 with an error of 1.5% [9]

$$\kappa_0^{Rb-^3He} = 4.52 + 0.00934[T(^\circ C)] \tag{2.43}$$

then it was measured by Babcock *et al.* in 2005

$$\kappa_0^{Rb} = 6.39 + 0.00914[T - 200(^\circ C)] \tag{2.44a}$$

$$\kappa_0^{K} = 5.99 + 0.0086[T - 200(^\circ C)] \tag{2.44b}$$

$$\kappa_0^{Na} = 4.84 + 0.00914[T - 200(^\circ C)] \tag{2.44c}$$

The two results agree within the error. Thus we can calculate ^{3}He polarization with the EPR frequency shift.

2.3.4 Experimental Methods

2.3.4.1 Overview

Under normal operating conditions, hybrid cells with mixture of Rb and K are used. The vapor density of K is an order of magnitude higher than that of Rb, we typically induce the $m_F = 2 \rightarrow m_F = 1$ (assuming the angular momentum of laser photons is +1) ^{39}K transition, which lowers the K polarization. Rb-K spin-exchange rate is fast enough that Rb is depolarized almost instantly. This allows more Rb atoms to absorb laser and be excited to the $5P_{\frac{1}{2}}$ state which in turn produces more D_2 fluorescence. The D_2 fluorescence is at maximum intensity when the RF frequency is on resonance for the Zeeman transition.

We first locate the frequency with a frequency-modulated (FM) sweep, and set the RF frequency to the found value. The RF is locked to the frequency (which is slightly changing) that induces maximum D_2 light with a proportional-integral feedback circuit (P.I. box). This frequency is referred to as EPR frequency and is measured with a counter. To separate the frequency-shifting effect of polarized ^{3}He from other sources that may affect the transition frequency, we flip the ^{3}He magnetization by performing a RF frequency sweep. A frequency sweep is chosen rather than a holding field sweep to keep external magnetic field constant, thus reducing factors that affect Zeeman splitting size. By comparing the frequency measured before and after the flip, together with the real temperature inside the pumping chamber, we can calculate the ^{3}He polarization. We typically take AFP measurements right before and after the relatively quick EPR measurement, so that a calibration constant that translates AFP signal size to ^{3}He polarization can be calculated.

2.3.4.2 Locating Zeeman Transition Frequency

The P.I. box only works well in locking the EPR frequency to the $m_F = 2 \rightarrow m_F = 1$ K transition when the EPR frequency is close to the transition. Thus the first step in EPR measurements is to locate the Zeeman transition. A frequency-modulated (FM) sweep is performed through a range that covers the Zeeman transition, the range is known from experience or calculation and the P.I. box remains off during the sweep.

The RF frequency is generated by the 18.2MHz voltage-controlled oscillator (VCO). The D_2 fluorescence is detected with the photodiode and recorded during the sweep. The RF is frequency-modulated by a 200Hz signal, the VCO output at any moment during the sweep can be described as:

$$V_{FM}(t) = V_{C0} \sin \left(2\pi[f_c + D_f \sin \left(2\pi f_m t + \phi_m\right)]t + \phi_c\right) \tag{2.45}$$

where V_{C0} is the amplitude of the sweeping RF frequency (carrier), f_c is the RF frequency that is being swept through a set range, D_f is the peak frequency deviation, f_m is the modulating frequency (200Hz in our case), ϕ_m and ϕ_c are the phase of the modulation frequency and carrier frequency, respectively. Thus the RF frequency is

$$f_{FM}(t) = f_c(t) + D_f \sin \left(2\pi f_m t + \phi_m\right) \tag{2.46}$$

here $f_c(t)$ emphasizes the RF frequency is sweeping over time.

The D_2 light intensity can be described with a Lorentzian function:

$$I(f(t)) = \frac{I_0}{(f_{FM}(t) - f_0)^2 + \Gamma^2} \tag{2.47}$$

where f_0 is the Zeeman transition frequency, Γ is the line width. Keeping the first order term of the Taylor expansion of Eq. 2.47, the D_2 light intensity is

$$I(f(t)) = I(f_c(t)) + \frac{\partial I}{\partial f}\bigg|_{f=f_c(t)} D_f \sin\left(2\pi f_m t + \phi_m\right) \qquad (2.48)$$

A lock-in amplifier is used to select only the f_m term and reduce the noise, the signal picked by the lock-in is

$$s(t) = \frac{\partial I}{\partial f}\bigg|_{f=f_c(t)} D_f \sin\left(2\pi f_m t + \phi_m\right) \qquad (2.49)$$

which is the derivative of the Lorentzian function multiplied by a sine function. The FM sweep line crosses zero when the RF frequency is equal to the Zeeman transition frequency (peak of the Lorentzian function), which produces the maximum D_2 light intensity. The region between the lowest and highest points of the derivative line is fitted to a line, and the zero-crossing point of the line is used as the Zeeman transition frequency. Fig. 2.7 shows an FM sweep.

2.3.4.3   EPR Spin Flip Process

After the transition frequency is located, the VCO frequency is first set to it and then stays locked with a proportional-integral feedback circuit (P.I. box). The circuit is shown in Fig. 2.8.

The output of the lock-in amplifier is sent to the input of the P.I. box, and the output of the P.I. box controls the input of the VCO. If the effective magnetic field drifts away from resonance, the P.I. box would receive a non-zero input, and attempt to change the frequency of the VCO output so that its input is zero again. Therefore,
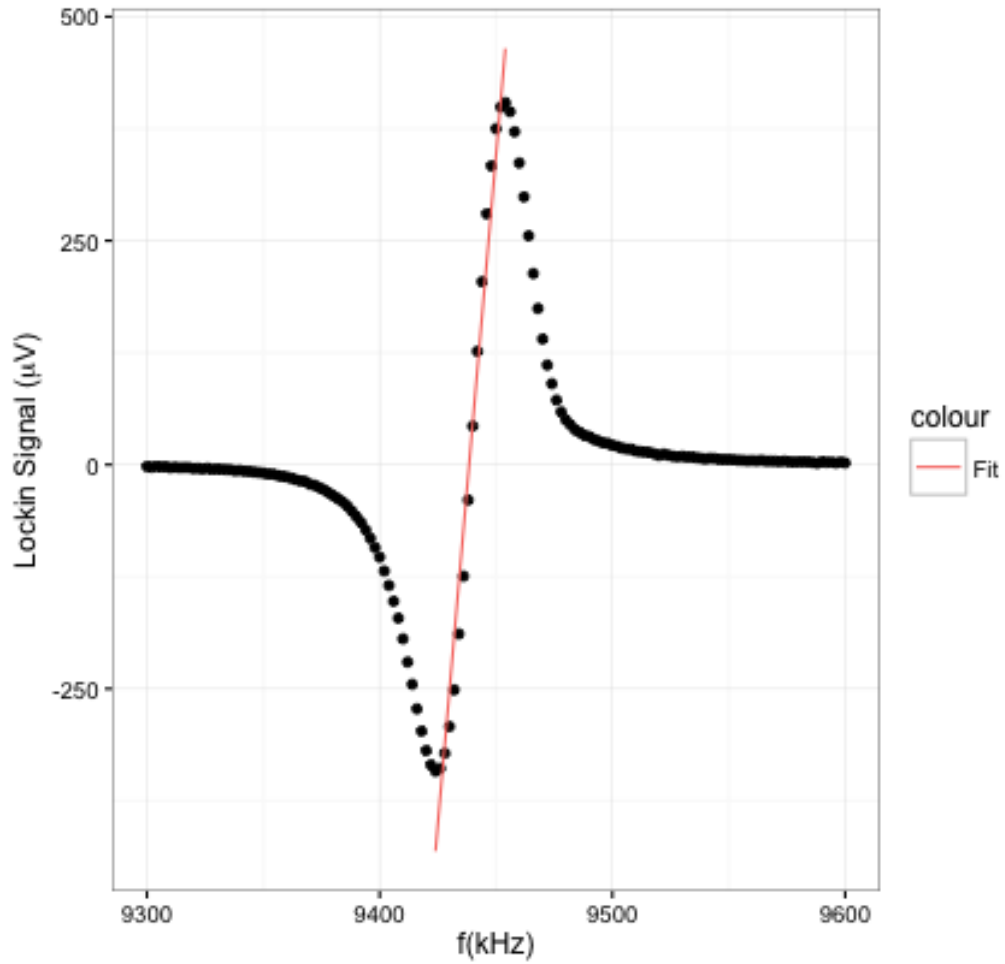
Figure 2.7: A typical FM sweep on a hybrid cell. The central region between the minimum and maximum is fitted to a line. The zero crossing point corresponds to the Zeeman transition frequency.

the VCO output always matches the transition frequency.

Because the EPR frequency is also affected by sources other than the polarized ^{3}He such as the holding field and earth field, we flip the ^{3}He spins by sweeping the frequency while keeping the holding field unchanged. The contribution from the flipped spins has a opposite sign while other factors still contribute in the same
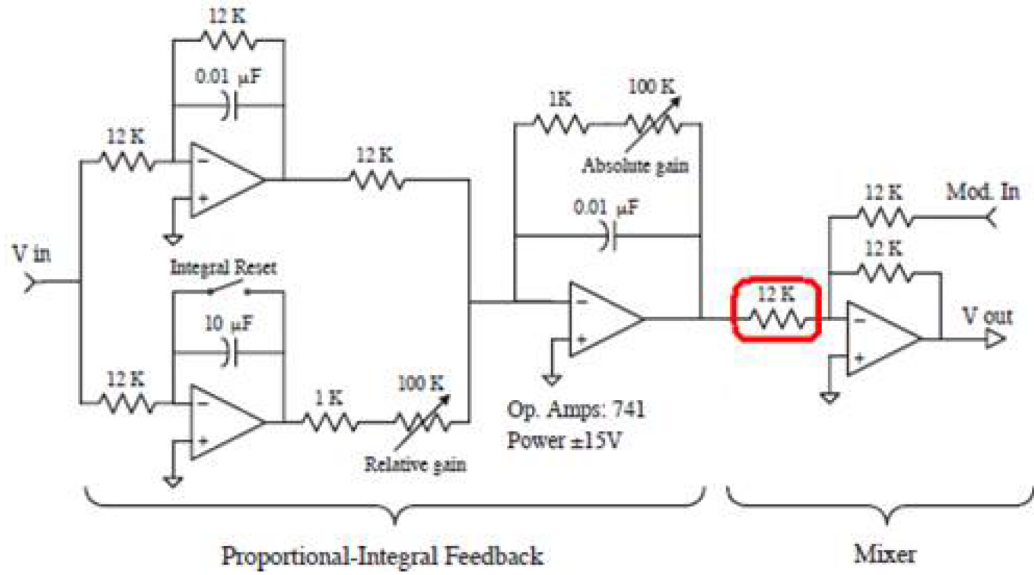
Figure 2.8: The same P.I. circuit that was first used by Romalis in our lab. The drawing was then corrected by Peter Dolph.[1]

way which allows us to extract the change of Zeeman transition frequency due to polarized ^{3}He and calculate the polarization. We typically let the cell polarization reach saturation before performing EPR measurements. AFP measurements are taken right before and after the EPR measurements for calculating the calibration constant (the ratio between polarization and AFP signal size). Fig. 2.9 shows a typical EPR spin flip process.

Under normal operating conditions for a double-chambered cell, the pumping chamber is heated to around 170°C or 235°C depending on if the cell is hybrid, the target chamber and transfer tube remain at room temperature. The temperature difference causes differences in gas densities and affects AFP signal size. Temperature controller of the oven only maintains the surface temperature of the pumping chamber at set temperature, but the gas inside the pumping chamber is always hotter due to
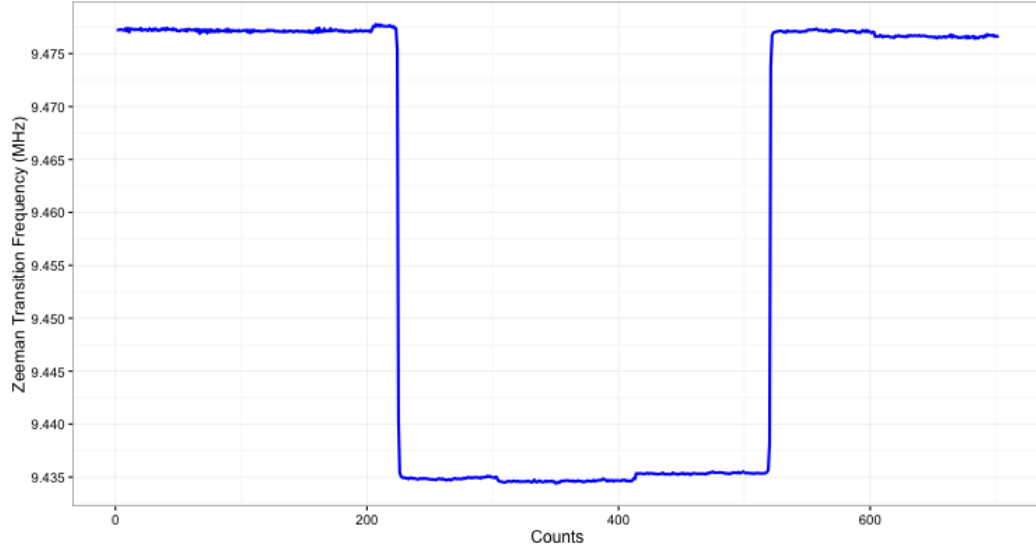
Figure 2.9: An EPR measurement for a hybrid cell at 235°C.

The spins are flipped around 200 mark, and flipped back around 500 mark.

absorption of laser energy. The enhancement factor κ_0 is also slightly temperature dependent which may be underestimated by $\sim 4\%$ when using the surface temperature as the gas temperature. Dolph described a method called temperature test to extract gas temperature inside the pumping chamber in detail in his thesis [1]. The idea is to take AFP measurements when the laser is blocked and unblocked multiple times, assuming the change of gas densities due to absorption of laser is the only reason for the difference in signal size (aside from AFP loss which is compensated through fitting) and the gas temperature when laser is blocked is the same as that measured by RTDs (resistance temperature detectors) on the exterior of the pumping chamber, one can calculate the inside temperature when laser is unblocked.

2.4 Pulsed Nuclear Magnetic Resonance

Adiabatic Fast Passage has been the main technique used in our lab for measuring ^{3}He polarization through detecting precessing spins with detection coils (we refer to them as pickup coils). In an AFP measurement, all ^{3}He spins are flipped by sweeping the holding field while applying a RF field. In more recent studies, we have been exploring the possibility of replacing conventional glass windows with metal end windows in response to the 12 GeV upgrade of JLab. Because of the lack of studies on spin relaxation of polarized ^{3}He on metal surfaces, various test cells made with large metal parts as well as glass parts are being studied in our lab. The inclusion of metal parts immediately renders AFP almost useless in the situation because of effects such as Eddy current, thus we have been performing Pulsed Nuclear Magnetic Resonance (PNMR) on metal cells.

2.4.1 The Rotating Coordinate System

In a PNMR measurement, a short pulse of RF frequency is applied to a small fraction of ^{3}He gas. The RF frequency is tuned to be on resonance at the Larmor frequency of the holding field. As discussed before with AFP, in the rotating coordinate system, there will be an effective field due to rotation that exactly cancels the holding field which we assume to be in the z direction. Thus the z component of the effective field is zero and there is a non-zero constant transverse component which we will call B_1. The nuclear spins will precess along B_1 and end up at an angle away from z axis:

$$\alpha = \gamma B_1 \Delta t \tag{2.50}$$

where α is the angle (tip angle), γ is the gyromagnetic ratio, and Δt is the RF pulse duration.

2.4.2 Free Induction Decay

At the end of the RF pulse, the tipped spins will have a transverse component equal to the magnetization multiplied by $\sin\alpha$. The spins continue to precess along the holding field and the transverse component will induce a signal in the pickup coils.

In addition to precession, the spins are affected by two types of relaxation processes. The first type is called the spin-lattice relaxation, it describes the rate at which the longitudinal component of magnetization approaches the thermodynamic equilibrium value. It is characterized by the spin-lattice relaxation time constant T_1. The rate of change of the longitudinal component is

$$\dot{M}_z = -(M_z - M_0)/T_1 \tag{2.51}$$

where M_0 is the thermodynamic equilibrium magnetization. Solving the differential equation gives

$$M_z(t) = M_0 - [M_0 - M_z(0)]\, e^{-t/T_1} \tag{2.52}$$

The name spin-lattice relaxation refers to the process in which the spins transfer energy to surrounding, thereby restoring their equilibrium state.

The second relaxation process is the transverse relaxation, which is also referred to as the T_2 relaxation and spin-spin relaxation. The transverse component of magnetization decays because variations in the local magnetic field cause different moments

to precess at different rates. This is the T$_2$ process. Normally, the dominating relaxation effect however, is another dephasing process due to inhomogeneities in the holding field over the volume of the cell.

The measured relaxation rate of the tipped spins is the result of all these effects combined:

$$\frac{1}{T_2^*} = \frac{1}{T_2} + \gamma \Delta B_0 \tag{2.53}$$

where ΔB_0 is the variation in the holding field. $\gamma \Delta B_0$, the dominant term, is a spread in Larmor frequencies $\Delta \omega_0$, which causes spin-spin dephasing in a characteristic time of $1/\Delta \omega_0$.

The time evolution of the nuclear magnetization $\mathbf{M}$ is described by the Bloch equations [3]:

$$\frac{\partial M_x(t)}{\partial t} = \gamma \left(\boldsymbol{M}(\boldsymbol{t}) \times \boldsymbol{B}(\boldsymbol{t}) \right)_x - \frac{M_x(t)}{T_2^*} \tag{2.54a}$$

$$\frac{\partial M_y(t)}{\partial t} = \gamma \left(\boldsymbol{M}(\boldsymbol{t}) \times \boldsymbol{B}(\boldsymbol{t}) \right)_y - \frac{M_y(t)}{T_2^*} \tag{2.54b}$$

$$\frac{\partial M_z(t)}{\partial t} = \gamma \left(\boldsymbol{M}(\boldsymbol{t}) \times \boldsymbol{B}(\boldsymbol{t}) \right)_z - \frac{M_z(t)}{T_1} \tag{2.54c}$$

where γ is the gyromagnetic ratio and the cross products are the precession terms, the last terms in each equation represent the decaying and dephasing of each component. The precessing spin magnetization generates a signal in the pickup coils that decays with time. This is called free induction decay, the induced signal is of the shape:

$$V(t) = A\omega_0 \sin \alpha \sin (\omega_0 t + \phi) e^{-t/T_2^*} \tag{2.55}$$

where A is just a constant, ω_0 is the Larmor frequency for the holding field, α is the tip angle, T_2^* is the measured decay time constant. For our metal test cells, depending on the location of the pickup coils and the field setup, T_2^* varies between several milliseconds to more than 300 milliseconds.

2.4.3 Experimental Methods

Our PNMR setup is shown in Fig. 2.10. The Labview program on the computer controls the timing of a gate signal that is fired from the first function generator. The gate signal is fed to the back of the second function generator and triggers it to produce a short pulse. The second function generator sends out RF pulse with pre-set amplitude, duration and frequency only when the gate signal is of voltage higher than the threshold. The frequency of the RF pulse is carefully tuned to be at the Larmor frequency of the holding field.

The pulse is sent from the function generator to a coil wrapped directly on a small portion of the cell. The spins contained in the coil are exposed to the pulse and tipped by an angle which depends on the amplitude and the duration of the pulse. In the rotating frame, the effective field B_1 causes the spins to precess around it (as discussed before), the precession frequency is γB_1 so the angle the spins rotate by (tip angle) is

$$\alpha = \gamma B_1 \Delta t \tag{2.56}$$
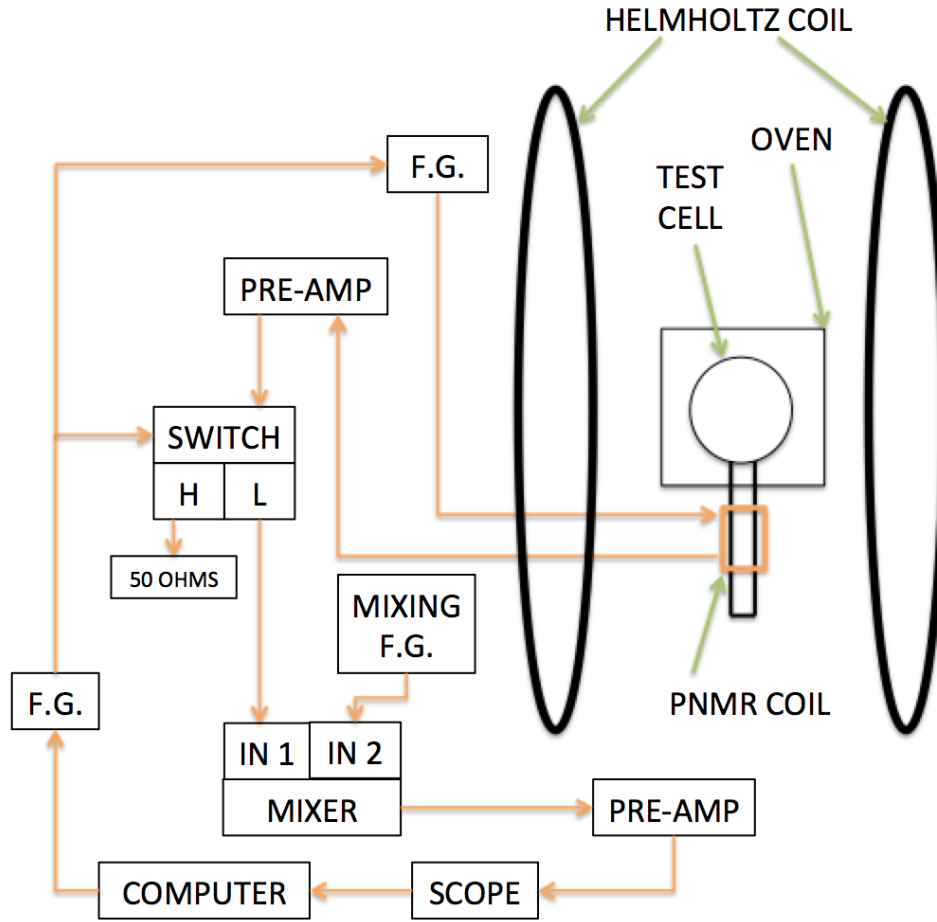
Figure 2.10: PNMR setup.

where γ is the gyromagnetic ratio, the effective field B_1 is directly proportional to the amplitude of the RF pulse, Δt is the duration of the pulse. Ideally, a 90° tip angle would result in the maximum signal, but it has not been the case for us most of the time because of field inhomogeneities. The coils are normally wrapped on the transfer tube of the cell which is off the center of the holding field and exposed to greater inhomogeneities. The details of how we measure the test cells will be discussed in later chapters. Relatively large inhomogeneities cause the spins to precess at different

rates, and the dephasing becomes more significant with longer pulse duration and larger tip angle, which leads to non-optimal signal. A typical tip angle for us would be between 30° and 45°.

After the spins are tipped away from z axis, they precess around the holding field and induce a signal in the detection coil. The signal is amplified by a low noise pre-amplifier first and then goes through an isolation switch. The switch only lets signal pass when the controlling gate voltage is low, thus stops the RF pulse from coming back through the detection circuit. The signal is at the Larmor frequency, and is mixed with another frequency after the switch. The mixing frequency is only slightly different from the Larmor frequency, the output of the mixer has both the sum of the two frequencies and the difference. A second pre-amplifier is used to select and amplify the lower of the two frequencies while filtering out high frequency noises. The final output is displayed on a oscilloscope and collected by the Labview program on the computer. Fig. 2.11 shows a PNMR measurement with around 150 ms decay time constant.
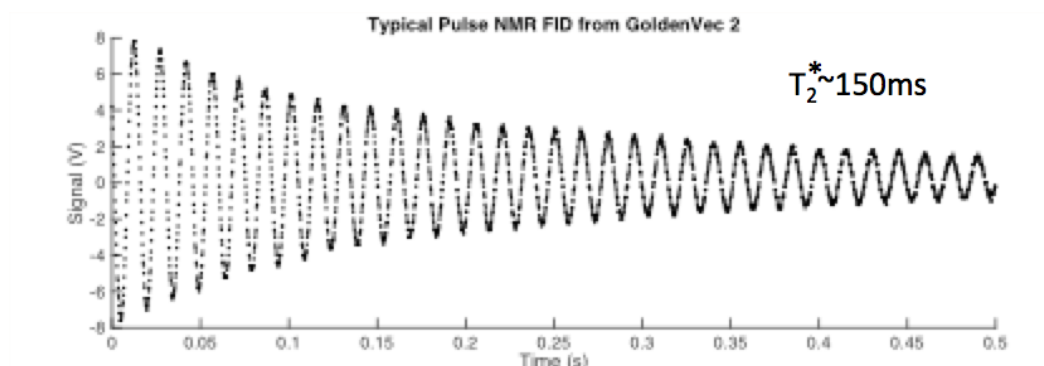
Figure 2.11: A PNMR signal taken with gold coated test cell.

The tip angle can be measured with a short sequence of FID signals. Theoretically the tip angle can be calculated with Eq. 2.56. But because of inhomogeneities and other factors, the calculation serves as only an estimate, it is often more accurate and convenient to measure the tip angle directly. We take several PNMR measurements in quick succession with the same RF pulse settings. After every pulse, the transverse component of the spins quickly decay and dephase, leaving only the longitudinal component which is equal to $\cos\alpha$ times the original magnetization. The intervals between measurements are short enough so that T_1 can be safely ignored. The series of measurements also need to be performed on the same portion of the gas (i.e. the same group of spins tipped by the first pulse), thus it is important to know that the self-diffusion of ^{3}He is significantly slower than the sampling rate. The self-diffusion coefficient of ^{3}He at 300K is [8]

$$D = \frac{1440(80)torr}{P}cm^2/s \tag{2.57}$$

which is roughly 1.89 cm^2/s at 760 torr (the test cells normally contain around 1 atm of ^{3}He). The diffusion length is described by

$$l = 2\sqrt{Dt} \tag{2.58}$$

Thus in one second, the gas will move around 2.75 cm through self-diffusion. For this reason, we only take 2 or 3 PNMR measurements to calculate the tip angle. As additional measurements would have given enough time for the tipped spins from the first PNMR and the surrounding spins to mix.

Since only the longitudinal component of the tipped spins are preserved, the am-

plitude of the i$_{th}$ PNMR is

$$V_i = V_0 cos^{i-1}\alpha \tag{2.59}$$

where V$_0$ is the induced signal in the first PNMR. We can then use this equation to calculate the tip angle α.

Chapter 3

Development of Hybrid Targets

3.1   Overview

In the first part of this chapter, I present the development of high-performance polarized ^{3}He targets for use in electron scattering experiments that utilize the technique of alkali-hybrid spin-exchange optical pumping. Data of 24 separate target cells are presented, each of these cells was constructed while preparing of one of four experiments at Jefferson Laboratory. The results document dramatic improvement in the performance of polarized ^{3}He targets. I focus on the data analysis work in this chapter since most of the data had already been taken by the time I joined the group. Other details are described by Jaideep Singh [**?**]. With the wide range of data, we successfully determined the so-called X-factors that quantify a temperature-dependent and as-yet poorly understood spin-relaxation mechanism that limits the maximum achievable ^{3}He polarization to well under 100%. We developed a simulation of the alkali-hybrid spin-exchange optical pumping process that provided a means to calculate volume

averaged alkali polarization. The data collected also served as a measurement of the K-^{3}He spin-exchange rate coefficient $k_{se}^K = (7.46 \pm 0.62) \times 10^{-20}$ cm^3/s over the temperature range 503 K to 563 K.

In the second part of the chapter, I report the results we have so far on developing the next generation target cell. As mentioned in previous chapters, target cells are composed of two distinct chambers: a pumping chamber (PC) where gas is polarized, and a target chamber through which the electron beam passes. The two chambers are traditionally connected by a single transfer tube. The polarization in the target chamber is replenished by gas from pumping chamber through diffusion. This is not a problem as long as the time scales associated with diffusion are short compared with the time scales associated with the depolarization process. The time scale of diffusion through transfer tube is roughly 0.5-1 hour. Due to the increasing electron beam current, the polarization gradient between the two chambers increased from 1-2% to up about 8% in more recent experiments. Future experiments are likely to use beam currents 4 times or more of what caused 8% polarization gradient. A new design was developed Peter Dolph which circulates the gas with convection instead of diffusion. Dolph demonstrated the design with a prototype cell, later I tested the first and second convection style cells with high ^{3}He polarization while having convection on. The success with our new design enables future experiment to run with higher electron beam current without causing too much polarization gradient.

3.2 Development of Targets without Convection

Spin-exchange optical pumping (SEOP) is a two step process in which an alkali-metal vapor is polarized with optical pumping which subsequently polarizes noble-gas nuclei via spin-exchange collisions. A pure Rb vapor was used to polarize ^{3}He prior to the development of hybrid cells. However, it was found that K is far more efficient than Rb at transferring its polarization to ^{3}He nuclei. Hybrid mixtures of Rb and K were used more and more frequently to improve the efficiency of the polarization process. In alkali-hybrid spin-exchange optical pumping (AHSEOP), the Rb vapor is polarized by circularly polarized laser, but the polarization of Rb valence electrons is then rapidly shared with the K. The rate at which Rb and K exchange polarization is so fast that their polarizations can be thought of as being equal. If the alkali-hybrid mixture contains significantly more K than Rb with appropriate ratio, the spin-exchange efficiency is greatly improved so that the rate at which ^{3}He is polarized is increased significantly for a given amount of laser power.

The second factor that proved to have improved target cells performance greatly was the use of spectrally-narrowed diode lasers. We were able to achieve higher alkali polarization with the aid of these lasers, which in turn reduced the required laser power. The origins of the improved cell performance are twofold. Firstly, these narrowband lasers have spectral profiles closely match the Rb D_1 absorption line shapes, which results in higher optical pumping rates and hence higher alkali polarizations. Secondly, it allows us to use higher alkali densities (which increases spin-exchange rates) without sacrificing alkali polarization.

The data collected over the years include ^{3}H polarization achieved under different

operating conditions, the time constants of polarization process, the geometric properties of the target cells, and cell fill information such as pressure and ratio of K to Rb in hybrid mixtures, the time constants of spin relaxation process. In roughly half the cells, the alkali polarization and alkali density were also measured with Faraday Rotation techniques. The results contain several thousand hours worth of data and provide valuable information for future cell development.

Two figures of merit (FOMs) are plotted in Fig. 3.1, both of which are relevant in evaluating the performance of a polarized ^{3}He target. The one on the left axis is the effective luminosity $\mathcal{L}^{eff} = \mathcal{L}P_{He}^2$, where $\mathcal{L}$ is the luminosity for a fixed-target experiment (the product of beam current, target density, and interaction length) and P_{He} is the ^{3}He polarization. The luminosity $\mathcal{L}$ represents the number of scattering opportunities per unit time per unit area, while P_{He}^2 accounts for the reduction in statistical error of some polarization-dependant asymmetry. The FOM on the right axis is used to quantify the potential effective luminosity of a target. The definition is $\mathcal{L}^N = \mathcal{N}\Gamma_s P_{He}^2$, where $\mathcal{N}$ is the total number of ^{3}He atoms in the target, Γ_s is the rate at which polarization builds up. The target cell Antoinette is the first one with such high value of $\mathcal{L}^N$, which indicates tis cell could tolerate higher luminosities than previously achieved. The high potential further demonstrates the importance of the development of the new convection style target cell. With even higher luminosities in electron scattering experiments, significantly faster gas transfer becomes quite necessary to reduce the polarization gradient between the pumping chamber of target chamber.
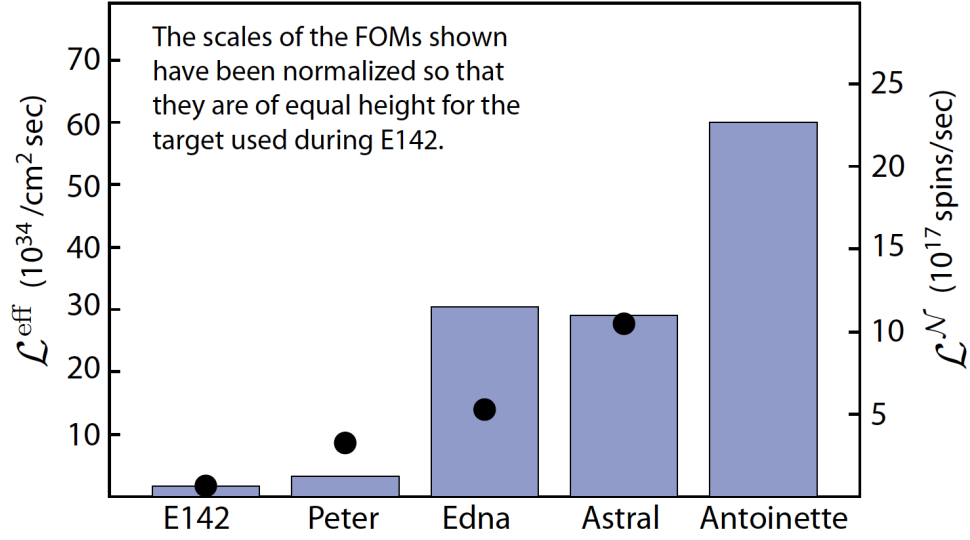
Figure 3.1: Shown are two figures of merit (FOM) for targets built for the indicated experiments. The circles (left axis) indicate the number of spins being polarized per second weighted by the square of polarization. The bars (right axis) represent the luminosity weighted by the square of polarization. While the first FOM is an indication of the potential of the polarization technique, the second FOM indicates performance achieved during an experiment. The actual cells used to formulate the FOMs are not necessarily the same.

3.2.1 Experimental Methods

3.2.1.1 The ^{3}He Targets

Chapter 2 has already described single-chambered cell polarization dynamics to some extent as it is a simpler model for introducing spin-exchange optical pumping. The ^{3}He target cells JLab uses for electron scattering experiments usualy include two chambers, a pumping chamber (PC), which is placed in an oven and pumped by

circularly polarized laser, and a target chamber (TC) that the electron beam passes through. Fig.3.2 shows a typical cell.
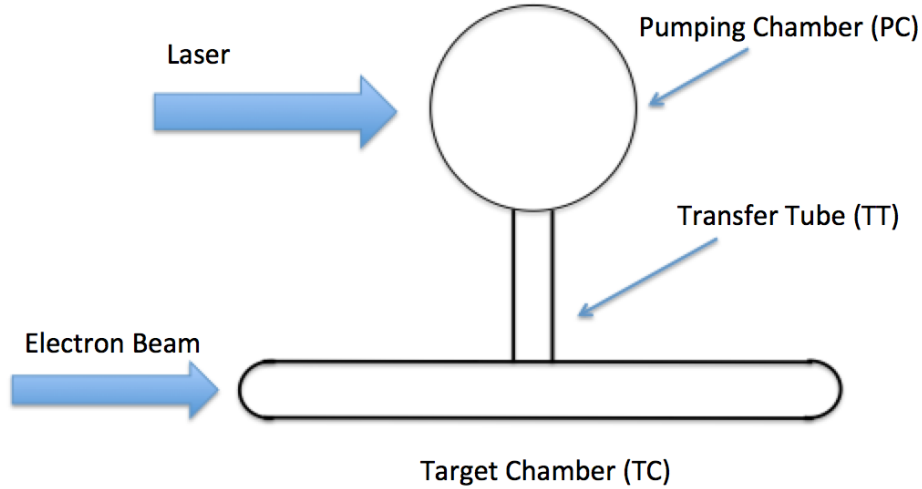
Figure 3.2: A target cell. The dimensions of different parts of the cell are not to scale.

After baking the cell to remove moisture and other contaminants, mixtures of Rb and K are chased into the cell. Once the cell has been pumped with a diffusion pump for about a week, we can fill the cell with N_2 and ^{3}He.

The ^{3}He density is of great importance for characterizing the target cells as it is required in many of the calculations I will discuss later in the chapter. One way to determine the ^{3}He density is to through measurements during the cell-filling process. A carefully calibrated volume, together with pressure and temperature measurements gives the volume of different spaces in the gas system (the system that is used to pump

the cell and fill it with N_2 and ^{3}He) and the cell. By comparing the amount of ^{3}He left in the system, the amount that went into the cell is obtained. The volume of the cell can be measured by determining its buoyancy force in water. The ^{3}He density is determined to within about 1% with the method.

Another method used quite often for determining the ^{3}He density through measurements of the pressure broadening of the D_1 and D_2 absorption lines with a scannable single-frequency laser. This measurement also provides the value of D, which is the ratio of K vapor density to Rb vapor density. Although the value of D is for the temperature at which the measurement is performed, its value for operating condition can be inferred with alkali-metal vapor pressure curves. D is also measured with the Faraday Rotation technique in many cases, and the two methods agree with each other quite well. The fill densities and geometric properties of the aforementioned 24 cells are shown in Table 3.1.

EXP	Cell	Total Volume(cc)	PC Volume(cc)	Fill Density(amg)	TC length(cm)
saGDH	Proteus	235.9	90.8	6.88	34.3
	Peter	208.6	111.3	8.80	39.4
	Penelope	204.3	102.2	8.93	39.7
	Powell	213.3	111.6	8.95	40.5
	Prasch	257.7	114.5	6.94	35.3
GEN	Al	168.4	90.2	8.91	38.4
	Barbara	386.2	306.8	7.60	38.7
	Gloria	378.2	298.8	7.40	38.4
	Anna	386.8	303.7	8.09	38.7
	Dexter	181.4	99.3	9.95	38.7
	Edna	378.3	290.3	7.47	38.7
	Dolly	378.3	293.5	7.42	38.7
	Simone	219.5	118.6	8.17	37.9
	Sosa	388.8	304.7	7.96	38.7
Transversity and d_2^n	Boris	246.1	166.1	8.08	38.4
	Samantha	259.0	176.9	7.97	38.4
	Alex	278.3	193.9	7.73	39.1
	Moss	269.8	184.7	7.92	38.7
	Tigger	271.7	186.9	7.81	38.7
	Astral	251.4	164.9	8.18	38.4
	Stephanie	244.3	164.9	8.10	38.5
	Brady	249.9	169.3	7.88	38.4
	Maureen	268.5	177.4	7.63	39.8
	Antoinette	437.8	351.8	6.57	40.3

Table 3.1: The table contains the names, total and pumping chamber volumes, fill densities and target chamber lengths of the 24 target cells. The fill densities are the average of the results from gas system measurements and pressure broadening measurements.

Bibliography

[1] High-performance nuclear-polarized ^{3}He targets for electron scattering based on spin-exchange optical pumping. *PhD thesis, University of Virginia*, 2010.

[2] E. Babcock, I. A. Nelson, S. Kadlecek, and T. G. Walker. ^{3}He polarization-dependent epr frequency shifts of alkali-metal˘^{3}He pairs. *Phys. Rev. A*, 71:013414, Jan 2005.

[3] F. Bloch. Nuclear induction. *Phys. Rev.*, 70:460–474, Oct 1946.

[4] G. D. Cates, S. R. Schaefer, and W. Happer. Relaxation of spins due to field inhomogeneities in gaseous samples at low magnetic fields and low pressures. *Phys. Rev. A*, 37:2877–2885, Apr 1988.

[5] G. D. Cates, D. J. White, T.-R. Chien, S. R. Schaefer, and W. Happer. Spin relaxation in gases due to inhomogeneous static and oscillating magnetic fields. *Phys. Rev. A*, 38:5092–5106, Nov 1988.

[6] E. M. M. V. Romalis and G. D. Cates. Pressure broadening of rb d_1 and d_2 lines by ^{3}he, ^{4}he, n_2, and xe: line cores and near wings. *Phys. Rev. A*, 56(6), 1997.

[7] I. I. Rabi, N. F. Ramsey, and J. Schwinger. Use of rotating coordinates in magnetic resonance problems. *Rev. Mod. Phys.*, 26:167–171, Apr 1954.

[8] M. L. R.Barbe and F. Laloe. Experimental verifications - measurement of the he3 self-diffusion coefficient. 35:935–951, 1974.

[9] M. V. Romalis and G. D. Cates. Accurate ^{3}He polarimetry using the rb zeeman frequency shift due to the Rb$-^3$He spin-exchange collisions. *Phys. Rev. A*, 58:3004–3011, Oct 1998.

[10] W. H. Thad G. Walker. Spin-exchange optical pumping of noble-gas nuclei. *RMP Colloquia.*

Appendix A

Appendix title

This is Appendix A.

You can have additional appendices too (*e.g.*, `apdxb.tex`, `apdxc.tex`, *etc.*). If you don't need any appendices, delete the appendix related lines from `thesis.tex` and the file names from `Makefile`.